Journal of Volcanology and Geothermal Research 417 (2021) 107298

Contents lists available at ScienceDirect

Journal of Volcanology and Geothermal Research

journal homepage: www.elsevier.com/locate/jvolgeores

Temperatures and water contents of Long Valley, CA basalts: Application of olivine–melt thermometry and hygrometry at the liquidus

Jameson S.R. Jolles *, Rebecca A. Lange

Department of Earth and Environmental Sciences, University of Michigan, Ann Arbor, MI 48109, USA

ARTICLE INFO

Article history:
Received 10 February 2021
Received in revised form 22 May 2021
Accepted 26 May 2021
Available online 29 May 2021

Keywords:
Basalt
Olivine
Olivine–melt thermometry
Olivine–melt hygrometry
Long Valley

ABSTRACT

The Plio-Quaternary Long Valley (LV) basalts, derived from subduction-modified lithosphere, are found in close proximity to the Long Valley caldera in California, from which hydrous high-SiO_2 rhyolites were erupted, including the climactic Bishop Tuff (>600 km^3). To better understand the processes by which the influx of basalts into the crustal column beneath Long Valley caldera led to the generation of voluminous high-SiO_2 rhyolite, it is necessary to determine the range of temperatures and water contents of the LV basalts. In this study, olivine–melt thermometry and hygrometry are applied to several, high-MgO (~7–10 wt%) LV basalts which contain phenocrysts of olivine and clinopyroxene, many of which display diffusion-limited, rapid-growth textures. Histograms of analyzed olivine compositions display a continuous, unimodal population in each sample. When the most Mg-rich olivine in each sample is paired with a liquid composition that matches that for the whole-rock (and a Fe^{3+}/Fe^T ratio of 0.24), ${}^{Fe^{2+}-Mg}K_D$ (olivine–melt) values of 0.32–0.36 are obtained, consistent with preservation of the first olivine composition to crystallize near the liquidus due to rapid phenocryst growth during ascent. Both a Mg- and Ni-based olivine–melt thermometer from the literature, calibrated on the same experimental dataset, were applied to the most Mg-rich olivine paired with the whole-rock melt composition. Because the Ni-thermometer is independent of water content, it provides the actual temperature at the onset of olivine crystallization in each of the LV basalts (1198–1053 °C), whereas the Mg-thermometer gives the temperature under anhydrous conditions and thus allows ΔT ($= T_{Mg}–T_{Ni} =$ depression of liquidus due to water) to be obtained. The average ΔT for all samples is 86 (±27) °C, which literature models show is consistent with an average melt water content of ~4.3 (±1.5) wt%.

1. Introduction

The Long Valley volcanic field in eastern California (Fig. 1), along the western margin of the Basin and Range extensional province, is well known for the eruption of high-SiO_2 rhyolite melts, including the Glass Mountain complex (~100 km^3) between 2.2 and 0.8 Ma (Metz and Mahood, 1991; Hildreth, 2004) and the supervolcano eruption (>600 km^3) of the Bishop Tuff (BT) at ~765 ka (Hildreth and Wilson, 2007; Andersen et al., 2017). The next most abundant magma type erupted in the vicinity, before and after the BT caldera-forming event, is mantle-derived basalt, referred to as the Plio-Quaternary Long Valley (LV) basalts (Bailey, 1989). The trace-element and isotopic compositions of these basalts support an origin by partial melting of subduction-modified lithospheric mantle (e.g., Cousens, 1996), perhaps triggered by upwelling asthenosphere in response to lithosphere thinning (i.e., Basin and Range extension) and/or delamination of lithosphere beneath the eastern Sierra Nevada batholith (Manley et al., 2000; Saleeby et al., 2003; Zandt et al., 2004; Putirka et al., 2012).

There is broad consensus that the origin of the voluminous high-SiO_2 rhyolite from the Long Valley region was driven by the influx of basalt into the crust (e.g., Hildreth, 1979; Bailey, 1989; Halliday et al., 1989; Hildreth and Wilson, 2007; Simon et al., 2014). Importantly, LV basalts were not only a source of heat, but also water. Notably, the Long Valley rhyolites contain high water contents (≤6.4 wt%; Wallace et al., 1999; Anderson et al., 2000; Roberge et al., 2013). These water contents could not have come solely from pre-existing granitoid crust, which only contains ≤0.6 wt% H_2O (in the form of biotite and hornblende;

---

* Corresponding author.
E-mail address: jjolles@umich.edu (J.S.R. Jolles).

https://doi.org/10.1016/j.jvolgeores.2021.107298
0377-0273/

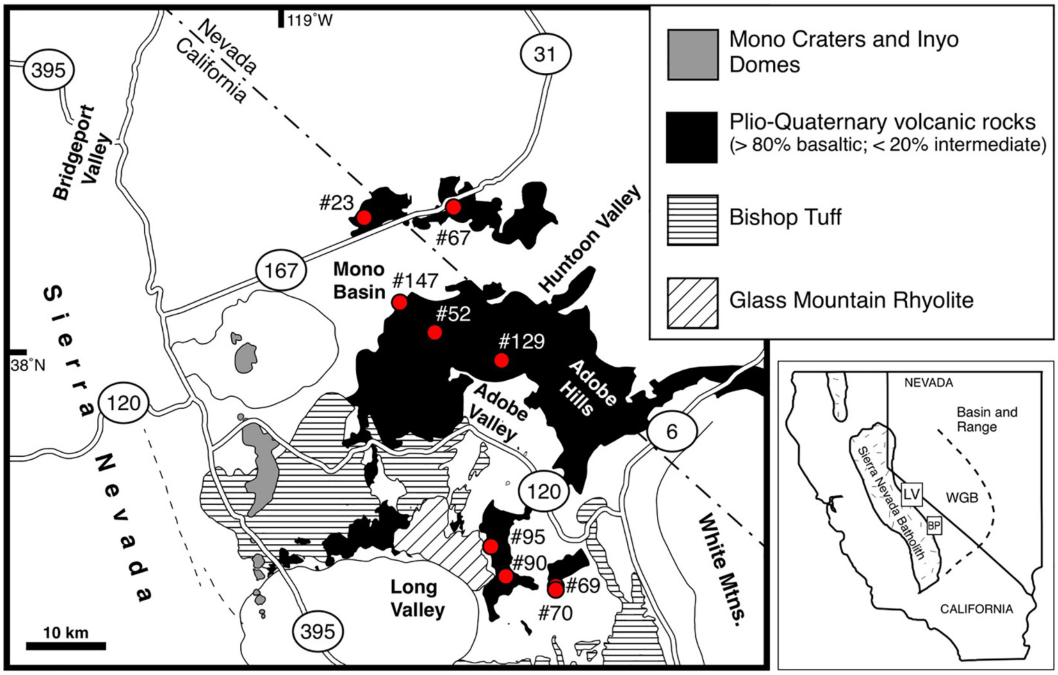

Fig. 1. Map of the Long Valley volcanic field and Adobe Hills, California, and surrounding area, adapted from Lange and Carmichael (1996). Black denotes Plio-Quaternary mafic lavas (predominantly basaltic) with sample locations (red circles). The inset map shows the location of Long Valley (LV) and Big Pine (BP) volcanic fields, along the western margin of the Basin and Range province and the Western Great Basin (WGB).

Bateman, 1992), but instead must have been derived primarily from the LV basalts. The numerical model of Calogero et al. (2020), which tracks the thermal evolution of the crustal column beneath the LV caldera due to the influx of basaltic sills, demonstrates the efficiency with which exsolved water from crystallizing basaltic sills can be transferred to partial melts in surrounding wall rock.

In order to better understand the processes by which the injection of basalt into the crust drove the formation of voluminous high-SiO_2 rhyolite at the Long Valley volcanic field, it is essential to document both the temperatures and water contents of the LV basalts at the time of their emplacement into the crust. Although the whole-rock major- and trace-element and isotopic compositions of the LV erupted basalts are well characterized (e.g., Cousens, 1996), only limited work has been done to establish their intensive variables (i.e., temperature, oxidation state, volatile content; Lange et al., 1993). In contrast, the Quaternary basalts erupted from the adjacent Big Pine volcanic field (located ~100 km south of the Long Valley caldera; Fig. 1) are well characterized, with known water contents (1.5–3.0 wt%) and Fe^{3+}/Fe^{T} ratios (0.24–0.25) obtained directly from analysis of olivine-hosted melt inclusions (Gazel et al., 2012; Kelley and Cottrell, 2012). In addition, olivine–melt thermometry, hygrometry, and oxybarometery have been applied to the Big Pine basalts (Brehm and Lange, 2020), leading to results that match those obtained from the melt inclusion analyses.

In this study, we follow the approach taken in Brehm and Lange (2020) and apply the Ni- and Mg-based olivinemelt thermometers of Pu et al. (2017) to the LV basalts. Because thermometers based on $D_{\mathrm{Mg}}^{\mathrm{ol/liq}}$ (e.g., Beattie, 1993) are strongly dependent on melt water contents (Almeev et al., 2007; Médard and Grove, 2008), they lead to temperatures that are too high for hydrous basalts and instead match those expected for anhydrous conditions at 1-bar. Conversely, thermometers based on $D_{\mathrm{Ni}}^{\mathrm{ol/liq}}$ are independent of dissolved water (Pu et al., 2021) and give temperatures for hydrous basalts that are below those obtained from the Mg-thermometer, consistent with dissolved water lowering liquidus temperatures. Therefore, when the temperature obtained from the Ni-thermometer (T_{Ni}) is combined with that from the Mg-thermometer (T_{Mg}), their difference ($\Delta T = T_{\mathrm{Mg}} – T_{\mathrm{Ni}}$) can be used to estimate melt water content (Pu et al., 2017, 2021). These results can be verified by comparison with $D_{\mathrm{Ca}}^{\mathrm{ol/liq}}$ values (at the onset of phenocryst growth), which correlate with dissolved water in the melt phase (e.g., Gavrilenko et al., 2016). The primary objective of this study is to apply these two olivine–melt thermometers to a suite of LV basalts in order to constrain both their temperatures and water contents at the onset of phenocryst growth, to help inform how the influx of basaltic magma into the crust drives the formation and eruption of voluminous high-SiO_2 rhyolite.

2. Sample locations, ages, and petrography

The location of the nine LV basalts that are the focus of this study are shown in Fig. 1. Four samples (#69, #70, #90, #95) are from isolated flows adjacent to the eastern margin of Long Valley caldera, another three (#52, #129, #147) are from the Adobe Hills, and the remaining two (#23, #67) are from the northern margin of the Mono Basin. Three of these nine samples – #23, #129, and #90 – were dated by the K–Ar method (Lange et al., 1993) with reported ages of 2.60 (± 0.06), 2.96 (±0.16), and 3.32 (±0.21) Ma, respectively. On the basis of the location and flow morphology of the remaining basalt samples from this study, it is estimated that they were largely erupted between 4 and 2 Ma, and thus Pliocene in age. These basalts are representative of the first mantle-derived melts to invade the crustal column after the volcanic hiatus in this region between 8 and 4.5 Ma (Bailey, 1989; Du Bray et al., 2016).

Table 1
Whole-rock major (wt%) and trace-element (ppm) concentrations and mineral modal proportions for Long Valley basalts.

Oxide (wt%)	#69	#52	#147	#95	#23	#90	#67	#70	#129
SiO_2	50.11	51.69	49.90	48.76	49.00	53.82	50.42	50.52	51.84
TiO_2	1.46	1.06	1.43	1.88	1.52	1.07	1.38	1.43	1.87
Al_2O_3	14.30	14.05	15.10	15.69	16.66	16.51	16.63	15.94	15.87
FeO^T	7.89	7.63	8.88	9.34	7.77	6.62	8.32	8.87	8.95
MnO	0.14	0.14	0.16	0.17	0.15	0.12	0.14	0.14	0.15
MgO	9.95	9.03	8.71	8.69	7.85	7.10	7.05	6.78	6.71
CaO	8.37	8.51	9.49	9.30	10.28	7.88	10.40	9.06	8.72
Na_2O	4.16	3.97	4.32	2.68	3.13	4.13	3.43	3.88	3.38
K_2O	2.89	2.41	1.40	2.75	2.63	2.18	1.68	2.84	1.95
P_2O_5	0.73	0.48	0.59	0.75	1.01	0.51	0.54	0.54	0.55
Original total	99.17	98.63	97.61	97.54	97.88	99.8	98.29	98.79	97.99
Mg#[a]	0.74	0.73	0.66	0.68	0.71	0.71	0.65	0.64	0.64
Trace element (ppm)									
Ni	213	227	122	141	115	144	69	49	105
Zr	234	157	152	241	243	177	153	171	199
Nb	13.7	9.2	17.5	19.5	18.5	12	11.7	10.9	20.3
Ba	1505	1690	1270	1195	1830	1640	1075	1485	1060
La	35	46	48	n.a.	40	n.a.	n.a.	28	32
Modes (vol%)[b]									
OLV phenocryst	8.2	5.0	3.4	7.1	2.6	5.3	1.7	2.2	3.2
CPX phenocryst	1.9	7.6	3.7	2.7	0.4	0.9	1.4	1.6	0.4
PLAG phenocryst	0.1	0.2	–	–	–	–	0.5	2.0	–

[a] Mg# = $(X_{MgO}/(X_{MgO} + X_{FeO}))$*100 and $Fe^{3+}/Fe^T = 0.24$ (see Section 5.1.2 Evidence that the most Mg-rich olivine in each sample is a near-liquidus phase).
[b] Modes represent ≥3000 point counts. Phenocryst ≥500 μm. OLV = olivine; CPX = clinopyroxene; PLAG = plagioclase. n.a. = not analyzed.

Olivine (≤7 mm) and clinopyroxene (≤4 mm) are the dominant phenocryst phases in these nine basalts, with plagioclase generally absent or subordinate (Table 1). Both sector and oscillatory zoning are clearly evident in several of the largest clinopyroxene phenocrysts in most samples. Phlogopite is found as a groundmass phase, nucleating on vesicle walls, in several flows. Small chromite crystals are common in the olivine phenocrysts and rare to absent in clinopyroxene phenocrysts. The groundmass is dominated by small grains of clinopyroxene and plagioclase, along with titanomagnetite. Ilmenite was not found in any of the nine samples, despite a targeted search for this phase.

3. Methods

3.1. Whole-rock major- and trace-element methods

The whole-rock major element composition of four of nine samples from this study (#23, #52, #90, #129) were previously reported in Lange et al. (1993). The major element compositions of the remaining five samples, along with the trace element compositions for all nine samples, were obtained by X-ray fluorescence (XRF) analysis at the University of California, Berkeley. Analytical uncertainty in the whole-rock Ni concentration, utilized for olivine–melt thermometry, is ±4 ppm.

3.2. Electron microprobe methods

Compositional analyses of olivine and clinopyroxene were obtained with the Cameca SX-100 electron microprobe in the Robert B. Mitchell Electron Microbeam Analysis Lab at the University of Michigan. The microprobe standards used for each element in each phase are presented in Table S1 (supplementary information). The analyses of olivine were made with a focused beam, an accelerating voltage of 15 kV, and beam current of 20 nA. Clinopyroxene analyses were made with a focused beam, an accelerating voltage of 20 kV, and a beam current of 20 nA. Olivine phenocrysts were analyzed in all nine samples, whereas clinopyroxene phenocrysts were analyzed in the three most Mg-rich samples: #52, #69, and #147.

For olivine, eight elements (Mg, Al, Si, Ca, Cr, Mn, Fe, Ni) were measured. Peak and background counting times were 30 s for Si, Mg, Fe, and

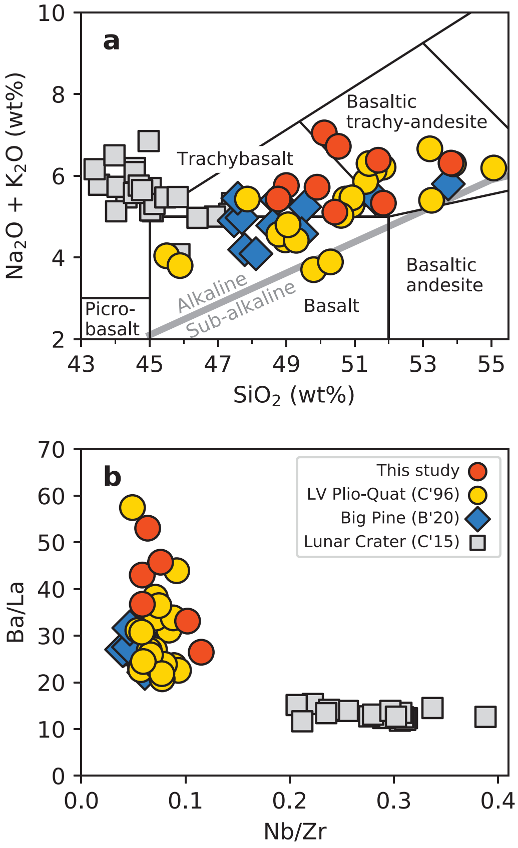

Fig. 2. (a) Whole-rock total alkalis ($Na_2O + K_2O$) versus silica for LV basalts (this study; Cousens, 1996), BP basalts (Brehm and Lange, 2020) and Lunar Crater basalts (Cortés et al., 2015), with zone boundaries from Le Maitre et al. (2005) and alkaline/sub-alkaline line from Miyashiro (1978). (b) Ratio of Ba/La versus Nb/Zr ratio. LV and BP basalts have an arc geochemical signature (enriched in slab-fluid component), consistent with subduction-modified lithosphere source, whereas Lunar Crater samples plot separately, consistent with asthenosphere source.

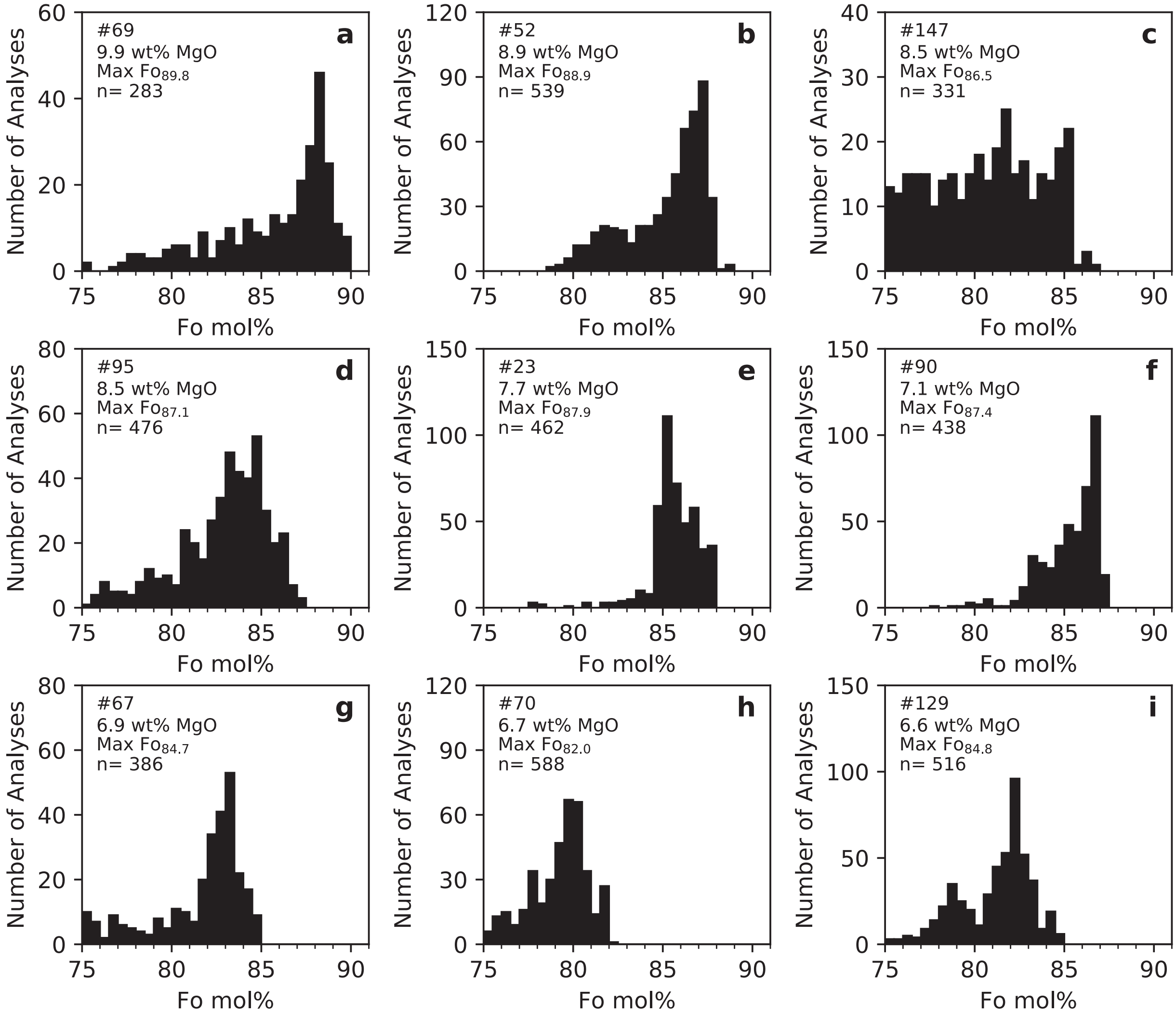

Fig. 3. Histograms of forsterite (Fo mol% = $X_{MgO}/(X_{MgO} + X_{FeO})*100$) content of olivine crystals for nine LV basalt samples. The most Fo-rich crystal in each sample was used for olivinemelt thermometry (Pu et al., 2017). Because only the most Mg-rich olivine crystals were targeted for analysis, histograms only represent the Mg-rich part of olivine population.

Table 2

Maximum Fo olivine composition; olivine–melt thermometry.

Oxide (wt%)	#69	#52	#147	#95	#23	#90	#67	#70	#129
SiO_2	41.00	40.80	39.85	40.31	40.53	40.37	40.06	39.37	40.42
Al_2O_3	0.03	0.02	0.02	0.04	0.04	0.00	0.02	0.02	0.01
FeO^T	9.68	10.59	12.89	12.18	11.44	12.22	14.34	16.79	14.27
MnO (calc.)[a]	0.14	0.13	0.16	0.16	0.18	0.15	0.22	0.22	0.18
MgO	48.00	47.38	46.29	46.22	46.69	47.50	44.65	42.87	44.61
CaO (calc.)[b]	0.16	0.14	0.15	0.20	0.21	0.10	0.20	0.21	0.15
Cr_2O_3	0.07	0.14	0.09	0.07	0.05	0.06	0.05	0.02	0.03
NiO (calc.)[c]	0.38	0.50	0.34	0.32	0.30	0.49	0.17	0.14	0.41
Total	99.53	99.78	99.81	99.40	99.46	100.88	99.72	99.61	100.08
max. Fo mol%[d]	89.8	88.9	86.5	87.1	87.9	87.4	84.7	82.0	84.8
Olivine–melt thermometry									
T_{Mg}°C[e]	1269 ± 7	1247 ± 7	1225 ± 7	1218 ± 7	1195 ± 7	1198 ± 7	1173 ± 7	*1187 ± 7*	1168 ± 7
T_{Ni} °C[f]	1198 ± 14	1165 ± 11	1098 ± 16	1136 ± 17	1116 ± 19	1101 ± 13	1132 ± 33	*1108 ± 42*	1053 ± 15
$\Delta T = T_{Mg}–T_{Ni}$ °C[f]	71	82	127	82	80	97	41	*78*	115
Min. melt H_2O (wt%)[g]	2.2	2.6	4.4	2.6	2.5	3.2	1.2	*2.5*	3.9
T_{Mg}°C (anhydrous): P'07[g]	1262	1240	1225	1219	1196	1185	1175	1186	1169
T_{Mg}°C (3 wt% H_2O): P'07[g]	1197	1176	1163	1157	1136	1127	1118	1128	1112
T_{Mg}°C (6 wt% H_2O): P'07[g]	1137	1119	1107	1102	1083	1074	1066	1075	1061
D_{Mg} (olivine–melt) mol%	3.8	4.1	4.2	4.2	4.7	5.2	5.0	5.0	5.2
D_{Mn} (olivine–melt) mol%	0.79	0.73	0.80	0.74	0.94	0.68	1.25	1.26	1.09
D_{Ca} (olivine–melt) mol%	0.015	0.013	0.013	0.017	0.016	0.010	0.015	0.019	0.014
D_{Ni} (olivine–melt) mol%	11	14	17	14	16	21	15	18	24

[a] MnO (calc.) from Fig. 6.

[b] CaO (calc.) from Fig. 5.

[c] NiO (calc.) from Fig. 4.

[d] Fo mol% = $(X_{MgO}/(X_{MgO} + X_{FeO}))*100$.

[e] T_{Mg} (±26 °C) and T_{Ni} (±29 °C) from the model of Pu et al. (2017); reported error is propagated from analytical uncertainty.

[f] Minimum melt H_2O wt% calculated using ΔT (Eq. 6) from Pu et al. (2017).

[g] T_{Mg} from Putirka et al. (2007). Thermometry results for sample #70 in italics, see Section 5.1.2 for application of olivine–melt liquidus test.

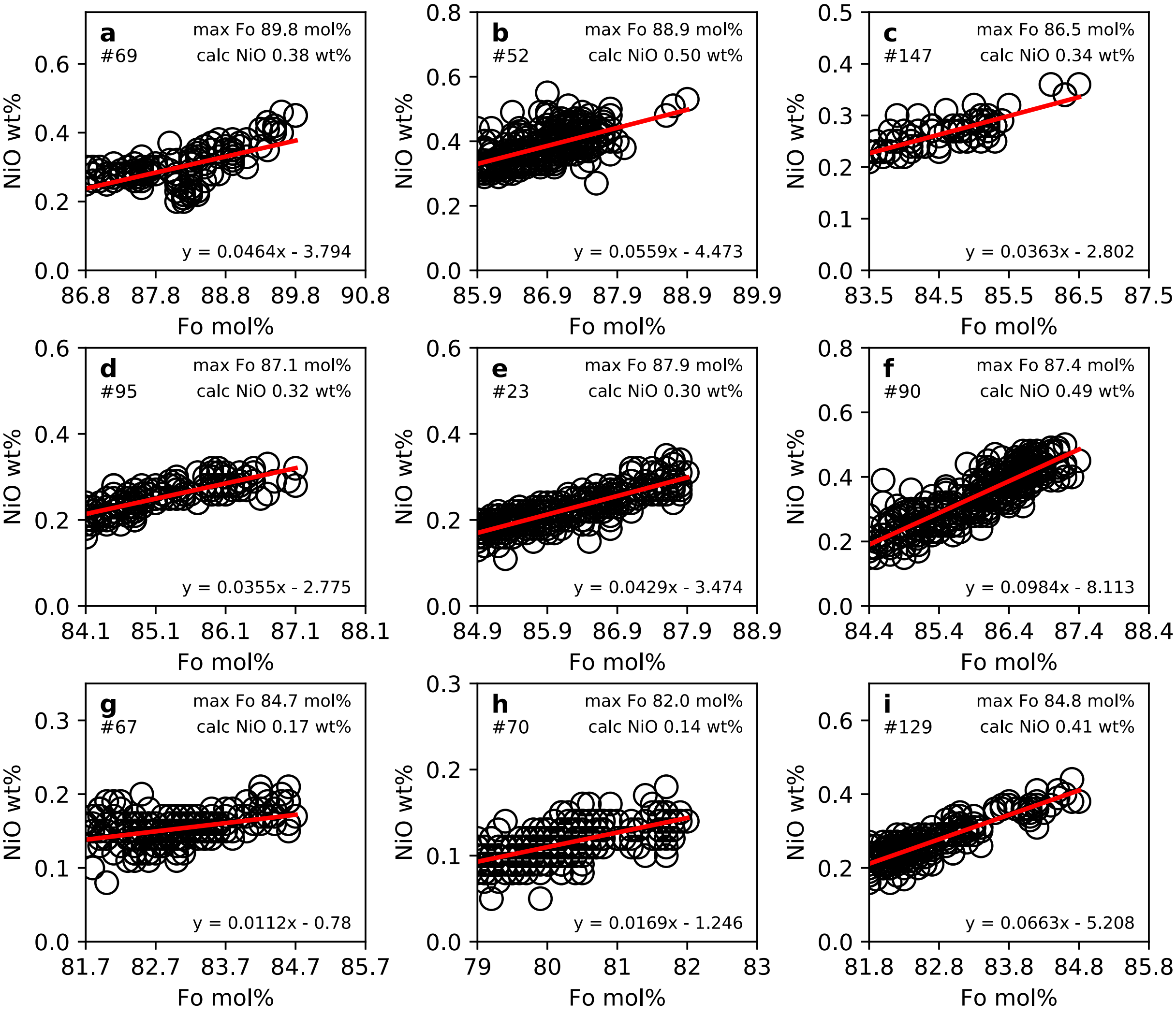

Fig. 4. NiO (wt%) in olivine versus Fo mol% for analyses of olivine that span the highest 3 mol% Fo in each sample. A linear fit to the top 3 mol% of the data in each sample (red line) is used to calculate the NiO wt% for the most Mg-rich olivine in each sample, which is used to calculate $D_{Ni}^{ol/liq}$ (mol%) for the Ni-thermometer. The most Mg-rich olivine composition (and calculated NiO wt%) are reported in Table 2.

Ni, whereas peak and background counting times of 20 s were used for Al, Mn, Cr, and Ca. The 1σ uncertainty for each oxide based on counting statistics is ±0.45 wt% SiO_2, ±0.30 wt% MgO, ±0.42 wt% FeO^T, ±0.02 wt% NiO, ±0.02 wt% Al_2O_3, ±0.01 wt% CaO, ±0.02 wt% Cr_2O_3, and ±0.05 wt% MnO. Analytical transects across 31–84 different olivine crystals were performed on each sample. Analyses were obtained every 25–80 μm, yielding 283–588 olivine compositions per sample.

For clinopyroxene, ten elements were measured (Mg, Al, Si, Ca, Cr, Mn, Fe, Ni, Na, Ti) Peak and background counting times were 30 s for Si, Mg, Fe, Ni, and Ca and 20 s for Al, Cr, Mn, Na, and Ti. The 1σ uncertainty for each oxide based on counting statistics is ±0.45 wt% SiO_2, ±0.17 wt% MgO, ±0.14 wt% FeO^T, ± 0.03 wt% NiO, ±0.12 wt% Al_2O_3, ±0.27 wt% CaO, ±0.03 wt% Cr_2O_3, ±0.06 wt% TiO_2, and ±0.03 wt% MnO. Analytical transects across 27–36 different clinopyroxene crystals were performed. Analyses were obtained every 25–135 μm, yielding 401–604 clinopyroxene analyses.

X-ray intensity maps of phosphorous (P) and iron (Fe) were obtained for the most Mg-rich olivine crystals in three LV basalts (#147, #95, and #23). An accelerating voltage of 20 kV and beam current of 200 nA were utilized with individual dwell times of 200–300 μsec. For one of these samples (#147), X-ray intensity maps of Mg, as well as aluminum (Al), titanium (Ti) and chromium (Cr), were obtained for two representative clinopyroxene phenocrysts. Back-scattered electron (BSE) images were obtained for several representative clinopyroxene phenocrysts in all three samples.

4. Results

4.1. Whole-rock major- and trace-element compositions

The major-element compositions of the basalts from this study are compiled in Table 1, together with selected trace element concentrations. The remaining trace element contents are compiled in a supplementary file (Table S2). The SiO_2 and MgO contents of the LV basalts from this study range from 48.8–53.8 wt% and 6.7–9.9 wt%, respectively. In a plot of total alkalis vs. SiO_2 (Fig. 2a), the LV samples plot in the trachybasalt field, largely because of their elevated K_2O contents (1.4–2.9 wt%; Table 1). For comparison, the Plio-Quaternary LV basalts from Cousens (1996; ≤10.05 wt% MgO) are shown in Fig. 2a, along with the Big Pine (BP) basalts from Brehm and Lange (2020).

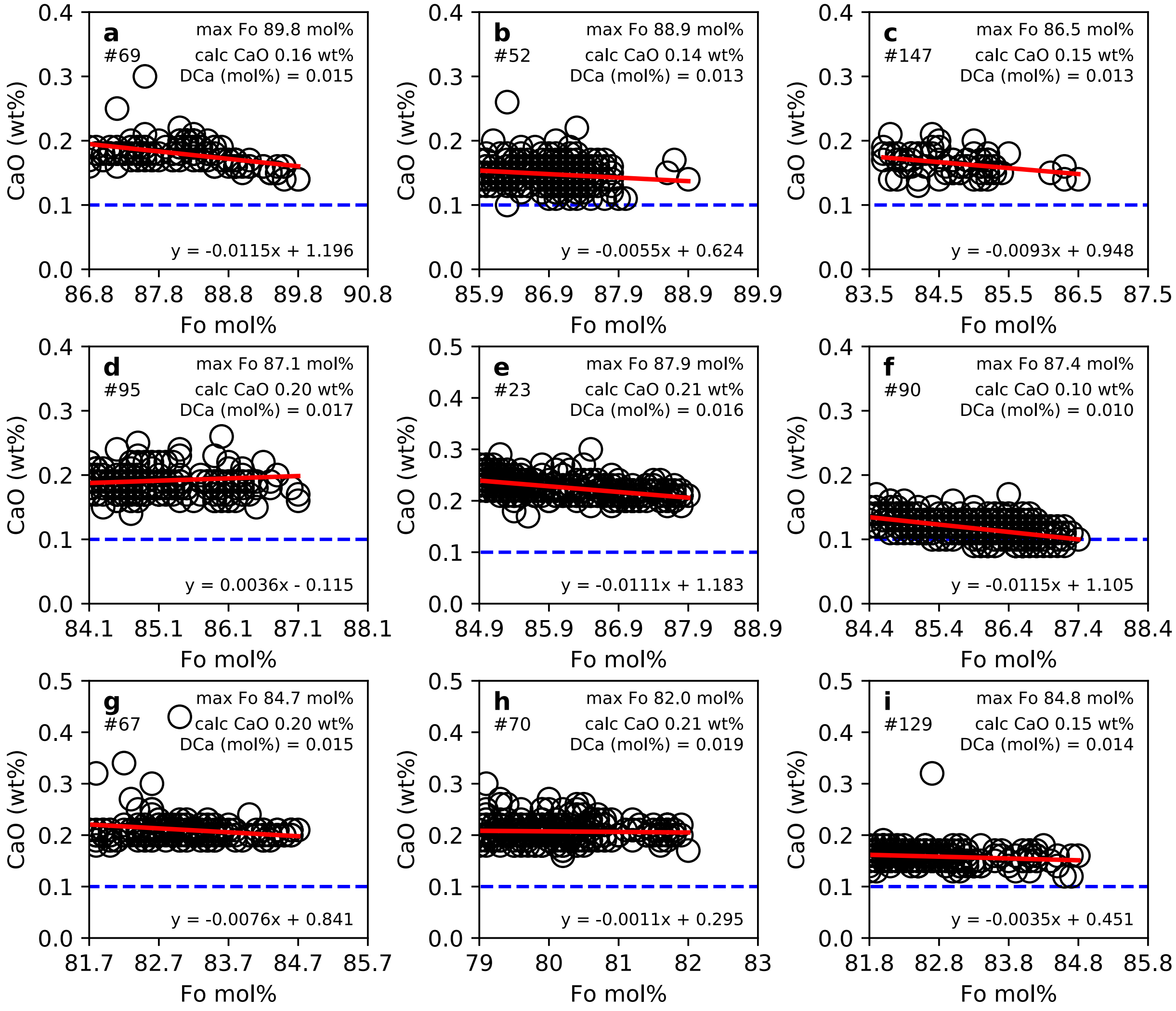

Fig. 5. CaO (wt%) in olivine versus Fo mol% for analyses of olivine that span the highest 3 mol% Fo in each sample. A linear fit to the top 3 mol% of the data in each sample (red line) is used to calculate the CaO wt% for the most Mg-rich olivine sample, which is used to calculate $D_{\mathrm{Ca}}^{\mathrm{ol/liq}}$ (mol%), reported in Table 2 and on each plot. Blue dashed line at 0.1 wt% denotes boundary between mantle olivine xenocrysts and phenocrysts (see Section 4.2 Olivine Results).

In a plot of Ba/La vs. Nb/Zr (Fig. 2b), the subduction-zone (i.e., slab-derived) signature of the LV and BP basalts is clearly seen in their elevated Ba/La ratios. For comparison, the trace-element ratios of several intraplate basalts from the Lunar Crater volcanic field, Nevada, (~250 km due east of the Long Valley region) are also shown, which are devoid of any slab-derived subduction signature (Cortés et al., 2015). The LV basalts from this study have Ba/La ratios that overlap and extend to higher values than those seen in the BP basalts (Fig. 2b). The trace-element signature of the LV basalts is consistent with an origin from subduction-modified lithospheric mantle (Cousens, 1996).

4.2. Olivine results

Individual analyses of olivine phenocrysts in each LV basalt sample are presented in Table S3 (supplementary information) and are shown as histograms of mol% Fo for each sample in Fig. 3. The results show a continuous range in composition (Fig. 3), and values of $D_{\mathrm{Mg}}^{\mathrm{ol/liq}}$ are calculated from the most Mg-rich olivine in each sample (Table 2) paired with the MgO content of the whole-rock sample (Table 1).

Plots of analyzed wt% NiO, CaO, and MnO as a function of mol% forsterite (Fo) for each sample are shown in Figs. 4, 5, and 6, respectively. The results in Fig. 5 show that the dominant olivine population in each sample contains ≥0.10 wt% CaO, in contrast to the olivine in mantle xenoliths from the Big Pine volcanic field (e.g., Beard and Glazner, 1995; Brehm and Lange, 2020). It is well established in the literature (e.g., Simkin and Smith, 1970; Norman and Garcia, 1999; Housh et al., 2010) that the low CaO content of olivine from mantle xenoliths can be used to distinguish between olivine xenocrysts and phenocrysts. For each sample, the wt% NiO, CaO, and MnO analyses that span the highest three mol% Fo were fitted to a linear relationship.

Application of the linear fit allows a more accurate estimate of the NiO, CaO, and MnO contents in the most Mg-rich olivine in each sample to be obtained (Table 2) because it eliminates the scatter due to analytical uncertainty. These values, when paired with whole-rock concentrations of NiO, CaO, and MnO, were used to calculate molar values of

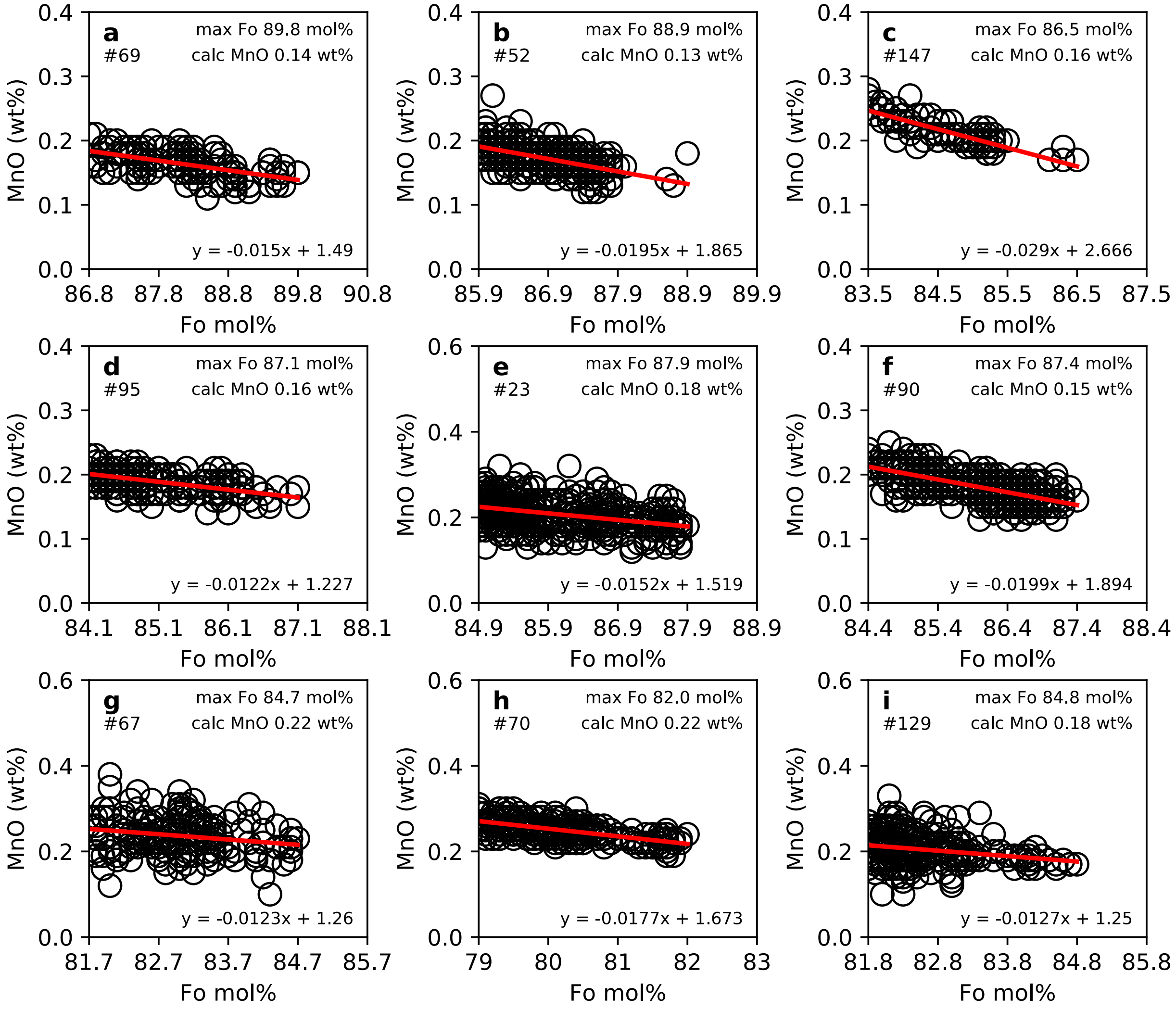

Fig. 6. MnO (wt%) in olivine versus Fo mol% for analyses of olivine that span the highest 3 mol% Fo in each sample. A linear fit to the top 3 mol% of the data in each sample (red line) is used to calculate the MnO wt% for the most Mg-rich olivine in each sample (Table 2), which is used to calculate the Mn–Mg exchange coefficient between olivine and melt at the liquidus (Table 3b).

$D_{Ni}^{ol/liq}$, $D_{Ca}^{ol/liq}$, and $D_{Mn}^{ol/liq}$ (Table 2). These partition coefficients are used later in the paper for olivine–melt thermometry and hygrometry (Table 2) and construction of $^{Mn-Mg}K_D$ (Table 3b; used to evaluate olivine–melt equilibrium).

X-ray intensity maps of P and Fe for Mg-rich olivine phenocryst in three representative LV basalts are shown in Fig. 7. All olivine crystals display complex P zoning patterns, consistent with rapid phenocryst growth. For comparison, a P map for olivine from a mantle xenolith (San Carlos, AZ), reported in Brehm and Lange (2020), shows no zones of P enrichment (Fig. 7i–j). Photomicrographs of representative olivine phenocrysts from six LV basalts are shown in Fig. 8.

4.3. Clinopyroxene results

Individual analyses of clinopyroxene phenocrysts in the three most Mg-rich samples (#69, #52, #147; Table 1) are presented in Table S4 (supplementary information). Plots of wt% TiO_2, Al_2O_3, Cr_2O_3, and Na_2O vs. Mg# for all clinopyroxene analyses from samples #69 and #52 are shown in Fig. 9 and from sample #147 in Fig. 10. Analyses of featured crystals in each sample are highlighted by colored symbols. In these three samples, there is no evidence of two compositionally distinct populations of clinopyroxene (e.g., high- and low-Na_2O), unlike the case in the Big Pine basalts (Brehm and Lange, 2020). The vast majority of clinopyroxene analyses in the LV basalts are characterized by relatively low Na_2O contents (<0.6 wt%).

The analyses in Figs. 9 and 10 are given different symbols based on the texture observed for each analytical spot along a transect: (1) sector and/or oscillatory-zoned; (2) dark, homogeneous core; and (3) patchy, diffuse, irregular. Examples of these textures are seen in BSE images (Fig. 11) and X-ray intensity maps of Mg, Al, Cr, and Ti (Fig. 12). The most abundant and common texture observed among clinopyroxene in all LV samples is sector and/or oscillatory zoning. The BSE images record sector zoning and oscillatory zoning patterns, both in large, discrete crystals (Fig. 11a–b), and as rims surrounding a dark, un-zoned core (Fig. 11c–e). The X-ray intensity maps for two phenocrysts from sample #147 (Fig. 12) show that sector zoning strongly affects Al, Ti, and Mg concentrations, but not Cr contents, whereas marked oscillatory zonation affects all four elements. Also shown is a rare xenocryst (Fig. 11f).

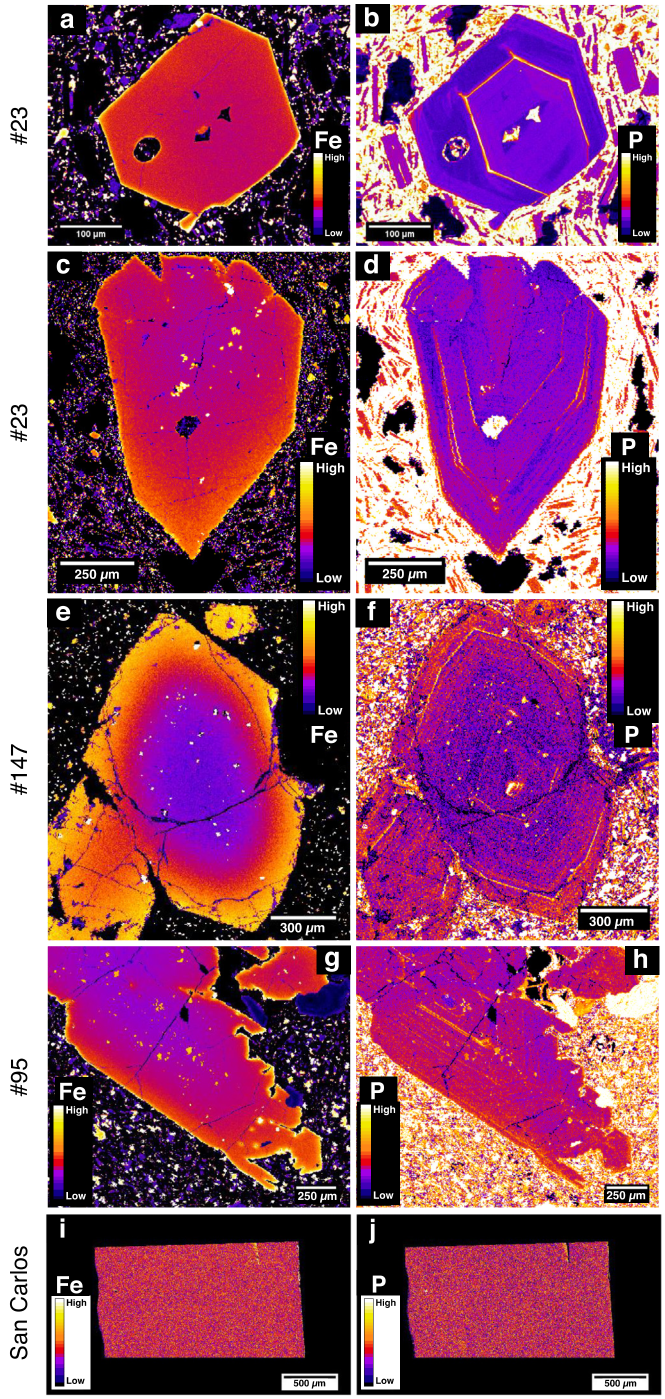

Fig. 7. X-ray intensity maps of Fe (left) and P (right) in Mg-rich olivine from three LV samples. Similar X-ray maps for an olivine from a mantle xenolith (San Carlos, Arizona) are shown for comparison. Complex P-zoning is associated with initial diffusion-limited rapid growth (e.g., Milman-Barris et al., 2008; Welsch et al. 2013; Welsch et al. 2014; Shea et al., 2019).

The analytical results show that the dark, un-zoned cores (Fig. 11c–e) have the highest Mg# and Cr_2O_3 contents (Figs. 9g and 10k) and are thus candidates for representing near-liquidus compositions. Notably, analyses from a single sector-zoned crystal (e.g., CPX 2 in sample #147; Fig. 10e–h) span nearly the entire compositional range as those from all sector-zoned crystals. There are marked compositional differences between different sectors in the zoned clinopyroxenes, and those with the higher concentrations of TiO_2 and Al_2O_3 (i.e., higher effective partition coefficients for Ti and Al) crystallized at faster rates (e.g., Kouchi et al., 1983). For the crystal with the xenocrystic texture (Fig. 11f), it has an interior that is low in Mg# and strongly depleted in TiO_2 compared to all other analyses (Fig. 10m). Analyses of the exterior to this crystal overlap those of the sector-zoned, phenocrysts, indicative of subsequent growth along its margins.

Photomicrographs of clinopyroxene phenocrysts from LV basalts (Supplementary Fig. S1) show that the most common clinopyroxene crystals display oscillatory- and sector-zoning. Dark, un-zoned cores are also commonly present. Therefore, the clinopyroxene results from the three samples analyzed appear to be broadly representative of all LV basalts from this study.

5. Discussion

5.1. Test of phenocryst growth in LV basalts during ascent

5.1.1. Evidence of diffusion-limited, rapid-growth textures in phenocrysts

Many of the phenocrysts in the LV basalts display diffusion-limited growth textures, including dendritic and/or hopper textures in the olivine phenocrysts (Figs. 7 and 8) and sector-zoning in clinopyroxene phenocrysts (Fig. 12). Such rapid-growth textures are expected for melts undergoing crystallization during an effective undercooling ($\Delta T_{eff\_uc} = T_{liquidus} - T_{melt}$) (e.g., Faure et al., 2003; Welsch et al., 2013; Shea et al., 2019). For hydrous basalts that initially segregate from their mantle source under fluid undersaturated conditions, initial ascent will lead to super-liquidus conditions because their liquidus temperatures will decrease with decreasing pressure. During continued ascent along fractures (Fig. 13), the effects of cooling, and eventually volatile degassing, will lead these basalts to cross their liquidus, but from a super-liquidus condition (e.g., Brehm and Lange, 2020). This will promote a kinetic delay to nucleation, allowing an effective undercooling to develop, which enables the growth of large, sparse phenocrysts (≤7 and ≤ 4 mm for olivine and clinopyroxene, respectively, in the LV basalts) owing to high crystal growth rates and low nucleation rates (e.g., Lofgren, 1974).

The complex P-zoning patterns observed in the LV olivine phenocrysts (Fig. 7) have been interpreted in the literature as recording an initial period of rapid, diffusion-limited, dendritic growth (Milman-Barris et al., 2008; Welsch et al., 2013, 2014; Shea et al., 2019). The lack of P zoning in the olivine from a mantle xenolith (Fig. 7j; Brehm and Lange, 2020) is consistent with a different growth history that did not include rapid crystallization from an undercooled liquid. Similarly, it has long been noted in the literature that sector zoning in clinopyroxene phenocrysts is also an indication of rapid-growth conditions (e.g., Shimizu, 1990; Brophy et al., 1999; Welsch et al., 2016; Ubide et al., 2019). For example, experimental studies demonstrate that sector zoning in clinopyroxene can develop at various undercoolings ($\Delta T_{eff\_uc} = 13–45$ °C), leading to rapid growth rates that range from ~0.14 to ~6.5 mm/day (e.g., Kouchi et al., 1983; Skulski et al., 1994). Thus, the clinopyroxene phenocrysts in the LV basalts may have crystallized within a few days or less. The X-ray intensity maps for the two clinopyroxene phenocrysts from sample #147 (Fig. 12) show that sector zoning and oscillatory zoning co-developed, which indicates that kinetic factors were likely involved in the development of both types of zoning.

5.1.2. Evidence that the most Mg-rich olivine in each sample is a near-liquidus phase

Pu et al. (2017) and Brehm and Lange (2020) showed that when phenocryst growth occurs rapidly during ascent (e.g., in basalts bearing mantle xenoliths), it is possible that the most Mg-rich olivine analyzed in each sample (Fig. 3) closely approximates the first phase to crystallize

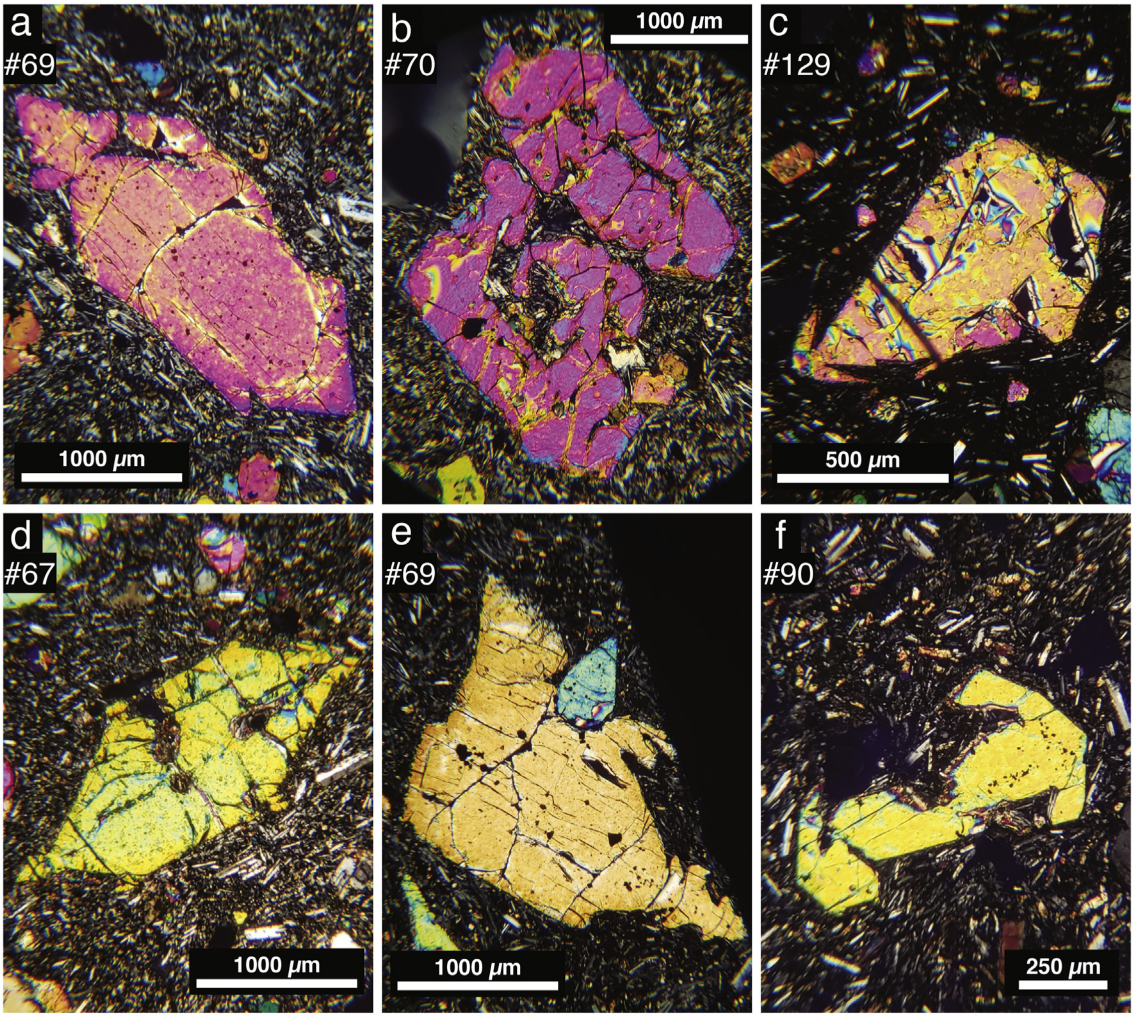

Fig. 8. Representative photomicrographs of olivine phenocrysts that display diffusion-limited growth textures from LV basalt samples, including hopper textures where the crystal grows faster at the edges of each face than in its interior (e.g., Donaldson, 1976; Faure et al., 2003).

from a liquid with a composition matching the whole-rock sample. In other words, when phenocryst growth during ascent is sufficiently rapid, the liquidus olivine composition may be preserved upon eruption. The fact that a wide range of olivine compositions is preserved in each sample (Fig. 3), indicates that there was not enough time for chemical re-equilibration of the entire olivine phenocryst population. Thus, an evaluation of whether the most Mg-rich olivine in each sample has the expected liquidus composition (i.e., the olivine–melt liquidus test) can be applied.

To perform this assessment, the most Mg-rich olivine phenocryst analyzed in each sample is plotted as a function of the whole-rock Mg#, as shown in Fig. 14. For the calculation of Mg#, it is assumed that the Fe^{3+}/Fe^{T} in each sample is 0.24, which is the average of micro-XANES analyses on olivine-hosted melt inclusions from Big Pine basalts (Kelley and Cottrell, 2012). Note that the Big Pine basalts share an arc geochemical signature with the LV basalts (Fig. 2). Superimposed on this plot are isopleths of ${}^{Fe^{2+}-Mg}K_D$ (olivine–melt) values:

$$ {}^{Fe^{2+}\text{-}Mg}K_D(\text{olivine–melt}) = \left(X_{Fe^{2+}O}/X_{MgO}\right)^{\text{olivine}} \left(X_{MgO}/X_{Fe^{2+}O}\right)^{\text{melt}} \quad (1) $$

The results show that the most Mg-rich olivine analyzed in the LV basalts overlap ${}^{Fe^{2+}-Mg}K_D$ (olivine–melt) isopleths that range from 0.32 to 0.36 for eight of nine samples (Table 3a; Fig. 14). The only exception is sample #70, which plots on a K_D isopleth of 0.39. The other eight samples have ${}^{Fe^{2+}-Mg}K_D$ values (0.32–0.36) that overlap those calculated with the MELTS thermodynamic model (Ghiorso and Sack, 1995; Asimow and Ghiorso, 1998), as well as the Putirka (2016) model (Table 3a). These models from the literature predict that variations in temperature, crustal pressure, and/or oxidation state do not lead to significant changes in ${}^{Fe^{2+}-Mg}K_D$ values for the LV basalts. Note, however, that Pu et al. (2017) presented evidence for a small increase in ${}^{Fe^{2+}-Mg}K_D$ value (≤0.03) with melt water (≤6 wt%). Calculated ${}^{Fe^{2+}-Mg}K_D$ values from this study, using the most Mg-rich olivine analyzed in each sample (Table 2), paired with the whole-rock composition (Table 1; $Fe^{3+}/Fe^{T} = 0.24$), are also given in Table 3a. The values match those of Putirka (2016), the most recently calibrated model, within ≤0.03 for all but one sample (#70), consistent with results illustrated in Fig. 14.

Also plotted in Fig. 14 are results from 10 basalts from the Big Pine volcanic field (Brehm and Lange, 2020), as well as 13 basaltic samples from the Mexican volcanic arc (Pu et al., 2017); all 23 of these samples plot on ${}^{Fe^{2+}-Mg}K_D$ isopleths that range from 0.31 to 0.37, based on a melt Fe^{3+}/Fe^{T} ratio of ~0.24 (close to the Ni–NiO buffer). Collectively, the results from these two volcanic fields, plus those for the LV basalts (eight

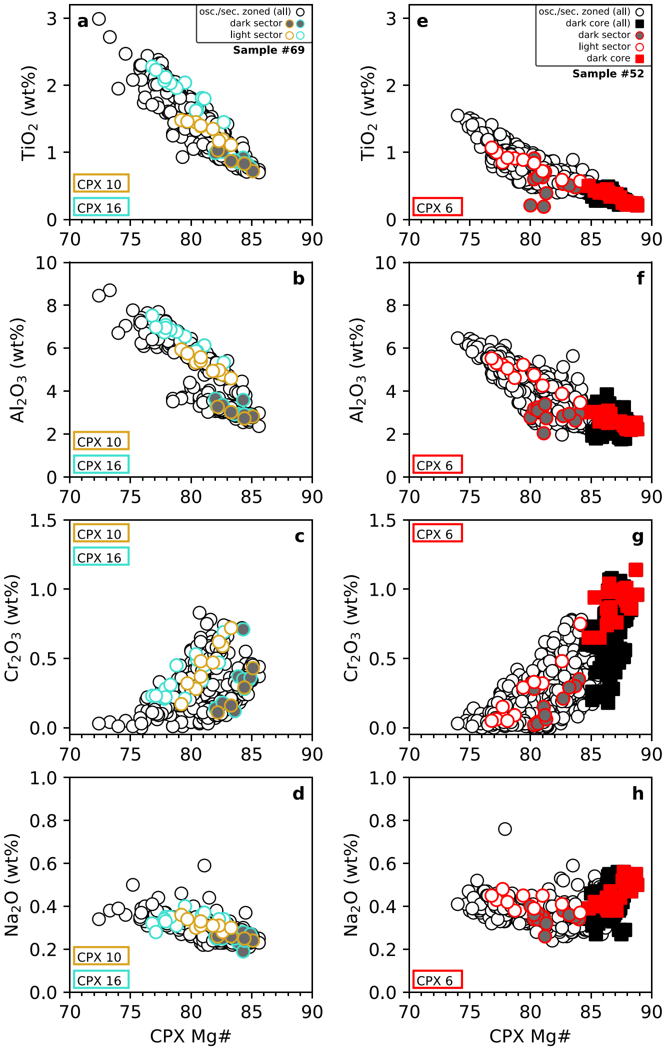

Fig. 9. Plots of TiO_2, Al_2O_3, Cr_2O_3, and Na_2O (wt%) vs. Mg# for CPX analyses from two LV samples (#69 and #52) with representative crystals highlighted (a–d) Analyses from sample #69; only crystals with oscillatory and sector zoning were found. As evidenced in highlighted crystals CPX 10 and 16 (Fig. 11a–b), each sector has distinctly different TiO_2, Al_2O_3, and Mg# ranges, but the same Cr_2O_3 contents. Note that the compositional range of the combined sectors (i.e., in a single crystal) spans nearly the entire compositional range for all clinopyroxene analyses. (e–h) Analyses from sample #52; many crystals had large, dark cores with zoned (sector and oscillatory) rims (e.g., CPX 6 plotted; Fig. 11c). The dark cores have the highest Mg# and Cr_2O_3 contents of the entire CPX population and is a candidate for a near-liquidus phase.

of nine samples), show that phenocryst growth during ascent and preservation of the first olivine composition to crystallize from the melt may be a common occurrence.

For the one sample from this study, #70, which appears to fail the olivine–melt liquidus test, several factors may be the cause. (1) The melt Fe^{3+}/Fe^{T} ratio for this sample may have been lower than 0.24 (slightly more reduced than measured in Big Pine lavas; Kelley and Cottrell, 2012); for example, a melt Fe^{3+}/Fe^{T} ratio of 0.17 at the liquidus of #70 leads to a ${}^{Fe^{2+}-Mg}K_D$ value of 0.36 (within ±0.03 of predicted literature values; Table 3a). (2) The most Mg-rich olivine in this lava may not have been exposed in the thin section. (3) Chemical re-equilibration of first-formed olivine may have occurred as crystallization progressed prior to eruption. (4) And/or olivine may not have been the liquidus phase in this basalt if the onset of phenocryst growth occurred at deep enough levels (and/or relatively low H_2O contents) to place clinopyroxene rather than olivine on the liquidus.

In summary, application of the ${}^{Fe^{2+}-Mg}K_D$ (olivine–melt) test shows that the most Mg-rich olivine analyzed in eight of the nine LV basalts matches the liquidus composition expected to crystallize from a liquid with the whole-rock composition. Therefore, application of olivine–melt thermometry to this pairing (most Mg-rich olivine and melt with whole-rock composition) will give the temperature at the onset of phenocryst growth in each of the eight basalts. With temperature in hand, an additional test of olivine–melt equilibrium at the liquidus can be made by applying the $RT\ln^{Mn-Mg}K_D$ (olivine–melt) model of Blundy et al. (2020; Eq. 10). The ${}^{Mn-Mg}K_D$ (olivine–melt) parameter is particularly valuable because it does not require that melt ferric-ferrous ratio be known. After temperatures are obtained, this additional test is applied below.

5.2. Olivine–melt thermometry

Numerous olivine–melt thermometers based on the partitioning of Mg ($D_{Mg}^{ol/liq}$) have been presented in the literature, and one of their critical limitations is that they are strongly sensitive to dissolved water in the melt (e.g., Almeev et al., 2007; Médard and Grove, 2008). Therefore, use of the Mg-based thermometer requires a correction for H_2O in the melt phase (e.g., Putirka et al., 2007), which also requires a priori knowledge (not always available) of the amount of water in the melt at the onset of olivine crystallization. In contrast, olivine–melt thermometers based on $D_{Ni}^{ol/liq}$ are independent of melt water contents (and pressure at crustal conditions; <1 GPa) and require no corrections (Pu et al., 2021).

Pu et al. (2017) calibrated two olivine-melt thermometers, based on the partitioning of Mg and Ni, on an identical set of 123 1-bar olivine-melt experiments. The two thermometers perform equally well, with 1σ errors for T_{Mg} and T_{Ni} of ±26 and 29 °C, respectively. The average (±1σ) temperature difference between the two thermometers (i.e., T_{Mg}–T_{Ni}) is 1 (±29) °C. Therefore, when both thermometers are applied to the same basalt, any difference in their calculated temperature >30 °C cannot be attributed to differences in their respective calibrations, and instead may reflect the role of dissolved H_2O in the melt. Because the Ni-thermometer is independent of dissolved water, it provides the actual temperature at the onset of olivine crystallization (Pu et al., 2021), and because the olivine liquidus is suppressed to lower temperatures (e.g., Almeev et al., 2007; Médard and Grove, 2008), calculated T_{Ni} values are consistently lower than T_{Mg} values in hydrous basalts (Pu et al., 2017, 2021). Importantly, the magnitude of the temperature difference (i.e., T_{Mg}–T_{Ni}) scales with the amount of water in the melt.

For the eight LV basalts that pass the ${}^{Fe^{2+}-Mg}K_D$ (olivine–melt) liquidus test and the one that does not, the Mg- and Ni-thermometers of Pu et al. (2017) were used to calculate temperature at the onset of phenocryst growth (Fig. 15). For the Mg-thermometer, values of $D_{Mg}^{ol/liq}$ were constructed from the most Mg-rich olivine in each sample paired with a liquid of its whole-rock composition and are reported in Table 2. Resulting temperatures from the Mg-thermometer (T_{Mg}) range from 1269 to 1168 °C for melts that range from 9.9–6.7 wt% MgO (Table 2; Fig. 15a). Analytical uncertainties in $D_{Mg}^{ol/liq}$, derived from the microprobe and whole-rock analytical errors, are relatively low (1–2%), and lead to propagated uncertainties in T_{Mg} of ±7 °C.

For the Ni-thermometer, values of $D_{Ni}^{ol/liq}$ were constructed for the most Mg-rich olivine in each sample based on a linear fit to the olivine data (wt% NiO vs. mol% Fo content) in Fig. 4. Resulting temperatures (T_{Ni}) range from 1198 to 1053 °C and are systematically lower than those obtained with the Mg-thermometer (Table 2; Fig. 15a). Analytical

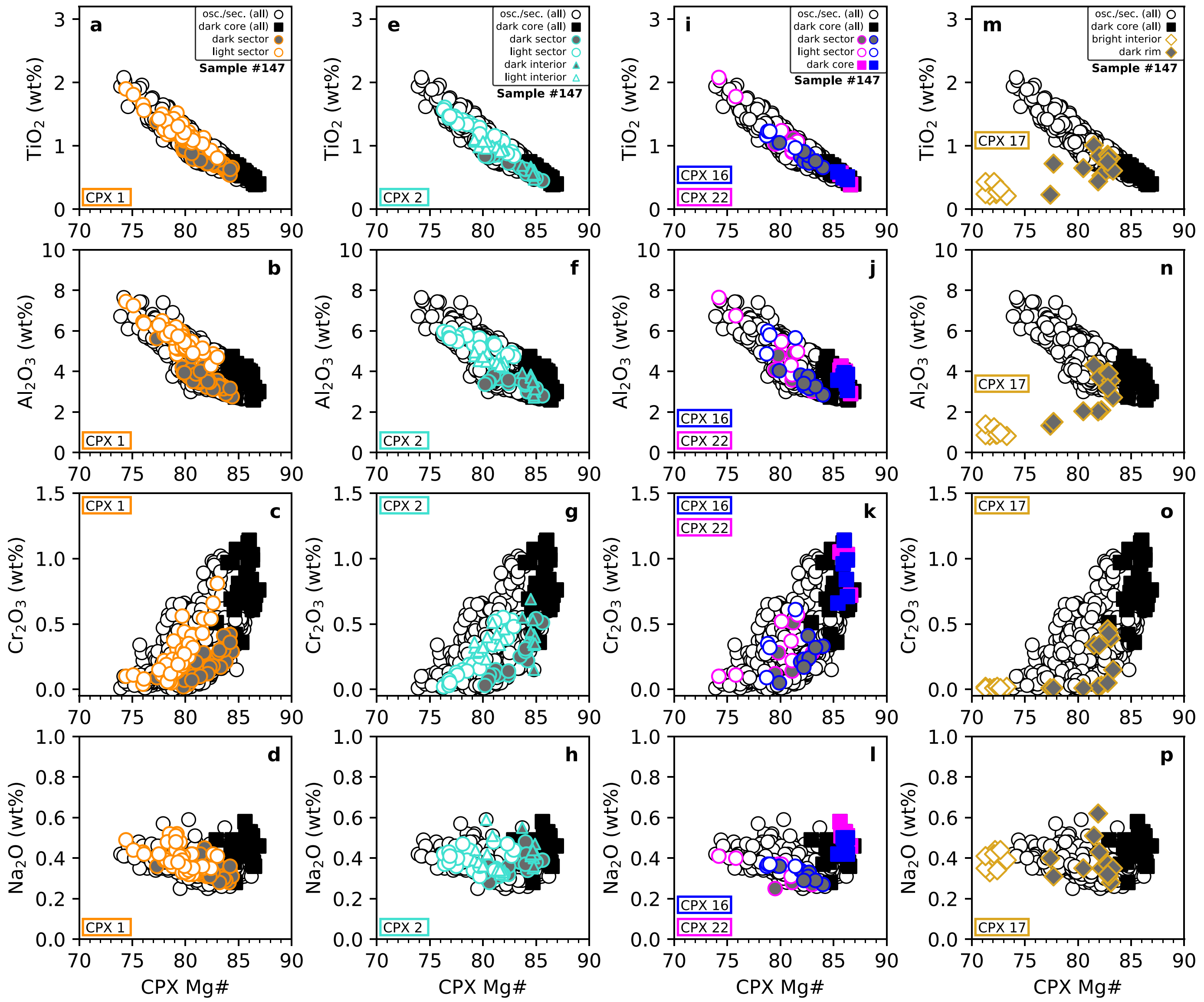

Fig. 10. Plots of TiO_2, Al_2O_3, Cr_2O_3, and Na_2O (wt%) vs. Mg# for CPX analyses from sample #147 with representative crystals highlighted. (a–d) Analyses of sector-zoned CPX 1 (Fig. 12a–d). Each sector (dark and light) has distinctly different TiO_2, Al_2O_3, and Mg# ranges, but the same Cr_2O_3 contents. Note that the compositional range of the combined sectors in CPX 1 (i.e., a single crystal) spans nearly the entire compositional range for all clinopyroxene analyses. (e–h) Same as (a–d) but for CPX 2 (Fig. 12e–h). (i–l) Compositional plots for clinopyroxene with dark core and zoned rim (CPX 16 and 22; Fig. 11d–e). The dark core has the highest Mg# and Cr_2O_3 contents of the entire clinopyroxene population. (m–p) Compositional plots for crystal with xenocrystic texture (CPX 17; Fig. 11f). TiO_2 and Al_2O_3 contents in the low-Mg# core are depleted compared to the rest of the clinopyroxene analyses, whereas rim compositions overlap other analyses, which suggests subsequent growth along margins on xenocryst.

uncertainties in $D_{Ni}^{ol/liq}$, derived from errors in the olivine (± 0.01–0.02 wt% NiO) and the whole-rock (±4 ppm Ni) compositions, lead to propagated uncertainties in T_{Ni} of ±11–19 °C for the seven samples with >100 ppm Ni. The uncertainties in T_{Ni} for samples #67 and #70 are larger owing to their lower whole-rock Ni contents: ±33 °C for sample #67 (69 ppm) and ±42 °C for sample #70 (49 ppm).

The results in Fig. 15a illustrate how temperatures based on $D_{Mg}^{ol/liq}$ (T_{Mg}) are systematically higher than those based on $D_{Ni}^{ol/liq}$ (T_{Ni}) and both systematically decrease with decreasing MgO content in the melt. The average temperature difference between the two thermometers (T_{Mg}–T_{Ni}) is ~86 (±27) °C (Fig. 15a), which points to the presence of dissolved water in the LV basalts.

5.3. Olivine–melt hygrometry

Similar, large differences in temperature (T_{Mg}–T_{Ni}) were obtained in Pu et al. (2017) and Brehm and Lange (2020), where both the Mg- and Ni-thermometers were applied to a suite of Mexican arc basalts and the Big Pine basalts, respectively (Fig. 15b and c). In those two studies, average ΔT (= T_{Mg}–T_{Ni}) values of 114 and 57 °C, respectively, were reported. Since values of ΔT (= T_{Mg}–T_{Ni}) scale with melt water content, the expectation is that the Mexican arc basalts were nearly twice as hydrous as the Big Pine basalts. This prediction is consistent with reported water analyses in olivine-hosted melt inclusions, with 3.9–5.7 wt% in the Mexican basalts (Johnson

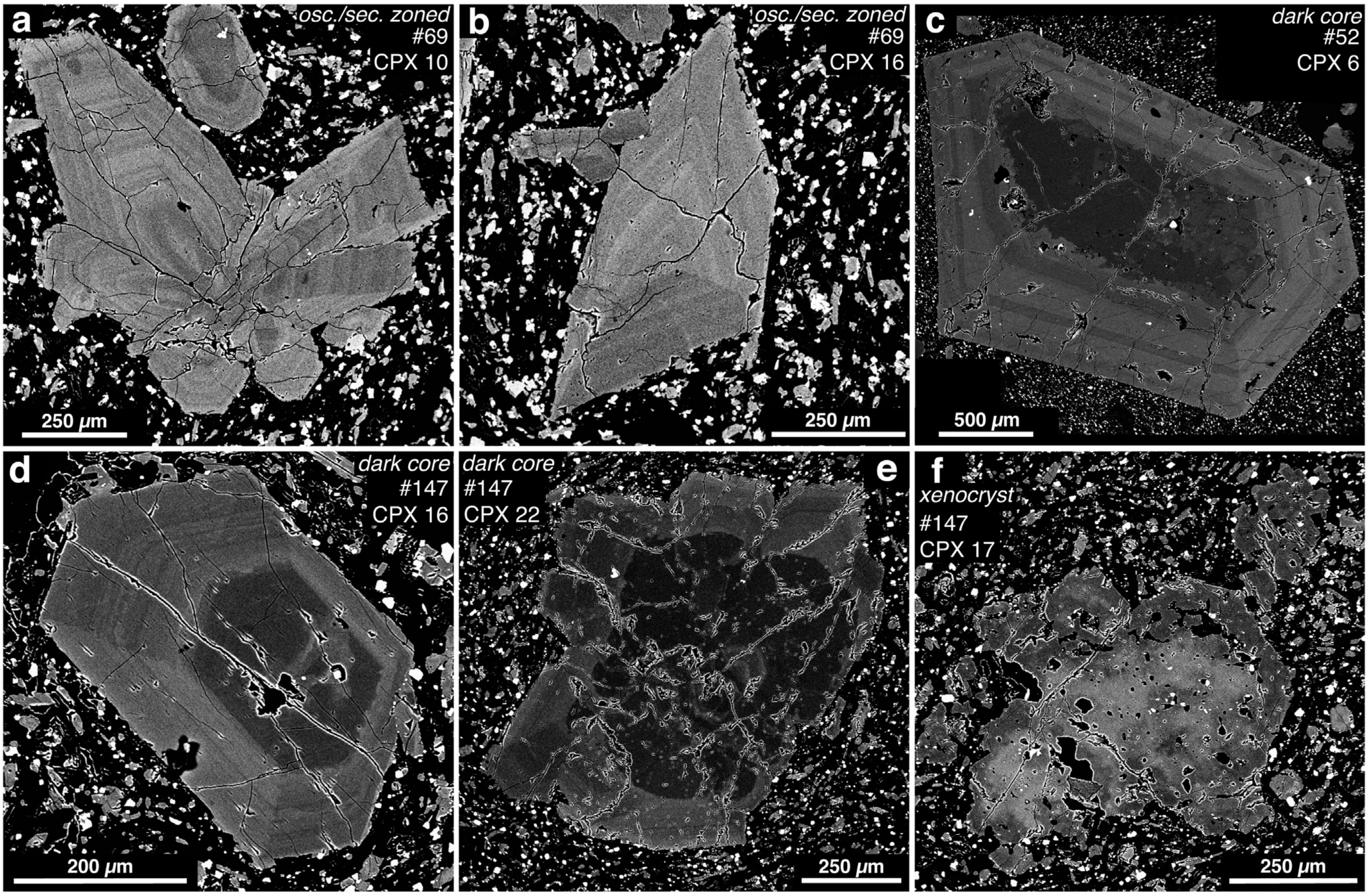

Fig. 11. Representative backscattered electron (BSE) images of clinopyroxene crystals from samples #69, #52, and #147. (a–b) Crystals with oscillatory and sector zoning (CPX 10 and 16 from sample #69; Fig. 9). (c–e) Crystals with dark core surrounded by oscillatory- and sector-zoned rim from samples #52 (Fig. 9) and #147 (Fig. 10). (f) Crystal (CPX 17; sample #147) with xenocrystic texture (mottled bright interior with dark margins).

et al., 2008; Johnson et al., 2009) and 1.5–3.0 wt% in the Big Pine basalts (Gazel et al., 2012).

Pu et al. (2017) provided a calibration of the relationship between melt water content and ΔT ($= T_{Mg}–T_{exp}$) values on the basis of 35 hydrous olivine–melt phase-equilibrium experiments from the literature and reported a polynomial that allows the minimum amount of water in the melt phase to reduce the liquidus by ΔT ($= T_{Mg}–T_{Ni}$) to be calculated. When this polynomial is applied to the average ΔT values of 114 and 57 °C for the Mexican arc basalts and the Big Pine basalts, respectively, minimum water contents of 3.9 and 1.7 wt% are obtained and consistent with those analyzed in olivine-hosted melt inclusions. When the polynomial from Pu et al. (2017) is applied to the average ΔT value of 86 °C obtained for the LV basalts, the average minimum water content is ~2.8 wt%. When the polynomial expression of Médard and Grove (2008) is applied, the average water content is also ~2.8 wt%. A further indication that these calculated dissolved water contents are minimum values is due to the fact that the Mg-thermometer has a pressure dependence, whereas the Ni-thermometer does not. For example, if the onset of olivine crystallization occurs at 0.5 GPa, the T_{Mg} value requires a correction of +26 °C (e.g., Herzberg and O'Hara, 2002; Pu et al., 2021). When this pressure correction is neglected, the resulting ΔT ($=T_{Mg}–T_{Ni}$) value is too low, which leads to a calculated water concentration that is also too low.

Another assessment of melt water contents can be made through application of the Putirka et al. (2007) Mg-based olivine–melt thermometer, which includes a correction for dissolved water content. In the absence of any H_2O correction, application of the Putirka thermometer to the LV basalts leads to calculated temperatures that closely match those obtained by the Pu et al. (2017) Mg-thermometer (Table 2). Inputting H_2O contents of 3–6 wt% into the H_2O-corrected Putirka et al. (2007) thermometer yields temperatures that recover T_{Ni} temperatures (Table 2; Fig. 15a), demonstrating good agreement with the Pu et al. (2017) thermometer. Note that these melt water concentrations are minimum values when a 1-bar pressure is chosen for the calculation. Brehm and Lange (2020) performed a similar exercise on the Big Pine basalts (Fig. 15b); it appears that the LV basalts contained ~50% more water than the Big Pine basalts.

Verification that the large, positive differences in $T_{Mg}–T_{Ni}$ (Fig. 15) reflect the effect of dissolved water in the melt phase can be made by examining $D_{Ca}^{ol/liq}$ values for various basalts with known and varying melt water contents. It has long been noted that CaO contents in olivine phenocrysts appear to be a strong function of dissolved water content, and Gavrilenko et al. (2016) have proposed that $D_{Ca}^{ol/liq}$ values can be used as an olivine–melt hygrometer. In this study, we compare average ΔT ($= T_{Mg}–T_{Ni}$) values and average $D_{Ca}^{ol/liq}$ values obtained for four sets of basalts: (1) the LV basalts from this study, (2) the Big Pine basalts (Brehm and Lange, 2020), (3) the Mexican arc basalts (Pu et al., 2017), and (4) the suite of mid-ocean ridge basalts (Allan et al., 1989) examined in Pu et al. (2017). Average ΔT ($= T_{Mg}–T_{Ni}$) values are plotted as a function of average $D_{Ca}^{ol/liq}$ values (Fig. 16)

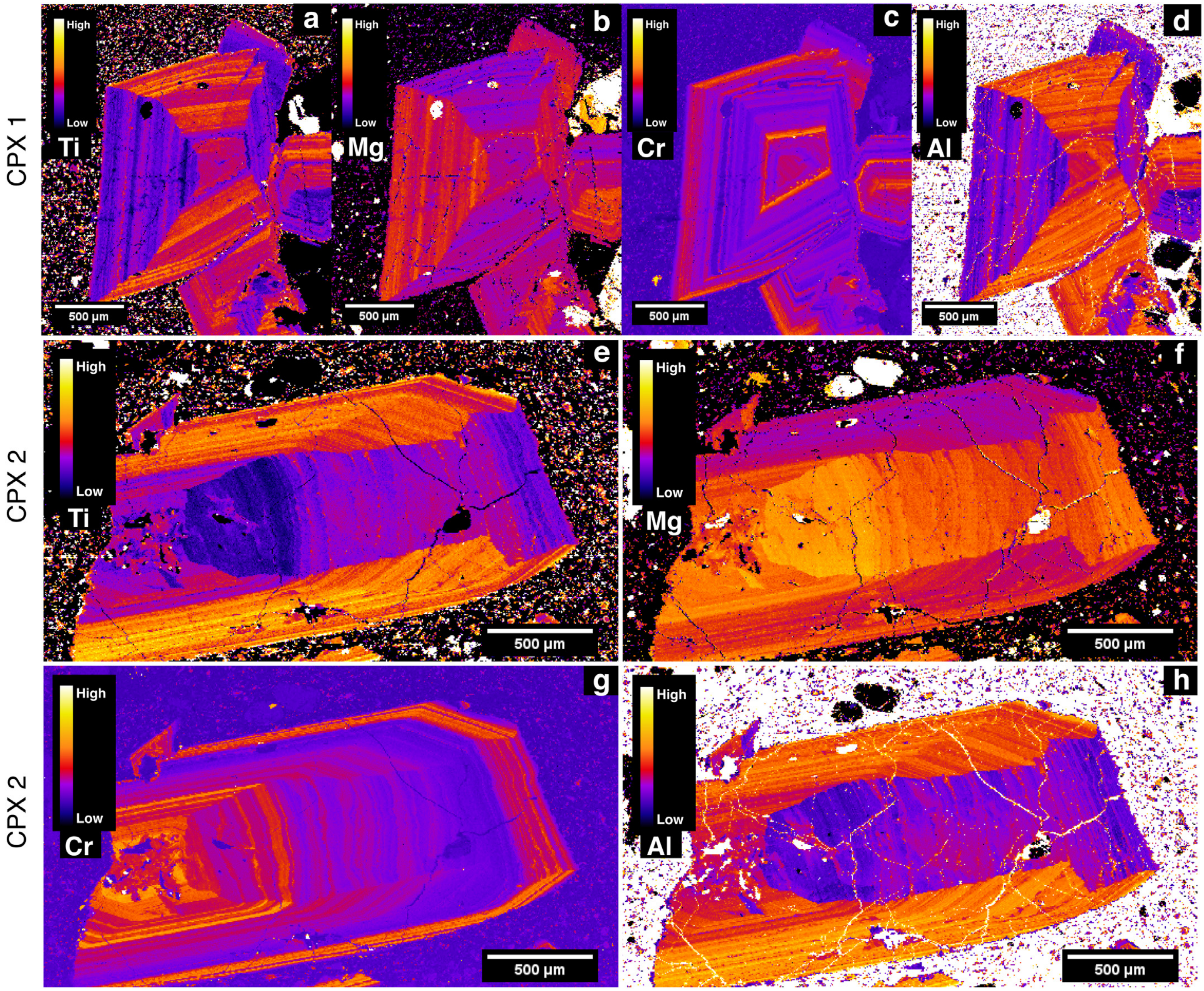

Fig. 12. X-ray intensity maps of Ti, Mg, Cr, and Al for two clinopyroxene crystals (CPX 1 and 2) from sample #147. Note sector and oscillatory zoning of Ti, Mg, and Al, whereas there is only oscillatory zoning of Cr.

and illustrate a strong, inverse linear ($R^2 = 0.99$) correlation. The highest $D_{Ca}^{ol/liq}$ values correspond to the mid-ocean ridge basalts from Allan et al. (1989), which are nearly anhydrous (~0.1 wt% H_2O), whereas those samples with the lowest $D_{Ca}^{ol/liq}$ values correspond to the Mexican arc basalts, which have the highest analyzed water contents (≤5.7 wt% H_2O; Johnson et al., 2009). As expected, the LV basalts and Big Pine basalts have $D_{Ca}^{ol/liq}$ values between the MORBs and arc basalts, consistent with melt water contents higher than those for mid-ocean ridge basalts, yet lower than those for active arc basalts. Moreover, the LV basalts have lower $D_{Ca}^{ol/liq}$ values compared to those in the Big Pine basalts, consistent with their higher minimum melt water contents (~2.8 vs. 1.7 wt%) that is predicted by their larger average ΔT ($= T_{Mg}–T_{Ni}$) values (~86 vs. ~57 °C). Thus, the $D_{Ca}^{ol/liq}$ values in Fig. 16 provide independent corroboration that the application of both the Mg- and Ni-thermometers from Pu et al. (2017) to basalts (with olivine compositions that pass the ${}^{Fe^{2+}-Mg}K_D$ liquidus test) provide accurate constraints on minimum melt water contents at the onset of olivine crystallization.

5.4. Additional evidence of Olivine-melt equilibrium at the liquidus

A final check on olivine–melt equilibrium at the liquidus can be made by utilizing the model equation of Blundy et al. (2020), which predicts values of ${}^{Mn-Mg}K_D$ (olivine–melt) on the basis of temperature and olivine composition. When the T_{Ni} values (Table 2) are combined with the most Fo-rich olivine analyzed in each sample (Table 2), calculated values of ${}^{Mn-Mg}K_D$ (olivine–melt) derived from the Blundy et al. (2020) model are obtained (Table 3a). These values can be compared to measured values of ${}^{Mn-Mg}K_D$ (olivine–melt) based on the data given in Tables 1 and 2. An error of ~0.03 is estimated for this measured ${}^{Mn-Mg}K_D$ value, and it is largely derived from the propagated analytical uncertainty in MnO concentration in the whole rock (±0.01 wt%) and

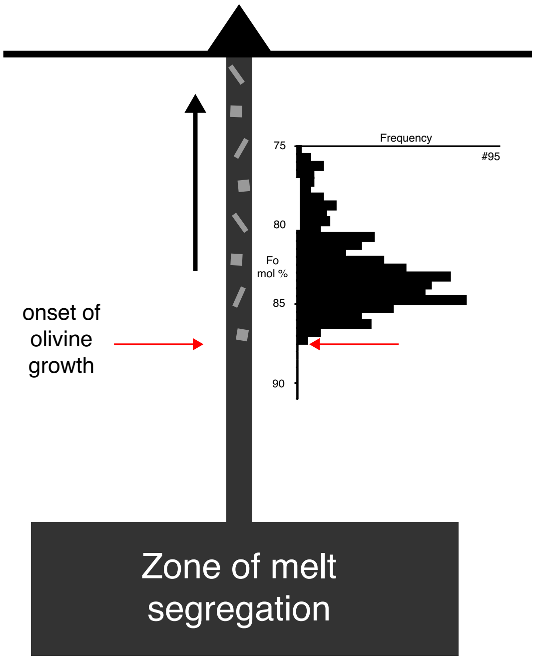

Fig. 13. Schematic illustration of phenocryst growth in basalt samples during ascent. It is proposed that the most Mg-rich olivine analyzed in each sample closely represents the first olivine to crystallize during ascent, when the $^{Fe^{2+}-Mg}K_D$ (olivine–melt) liquidus test is passed. In each case, olivine–melt thermometry can be applied using the whole-rock for the liquid composition, and the calculated temperature (T_{Ni}) is for the onset of olivine crystallization during ascent.

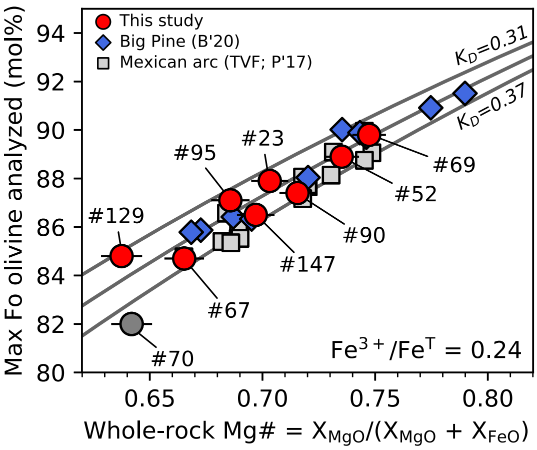

Fig. 14. Plot of most Mg-rich olivine composition (mol% Fo) analyzed in each LV sample versus Mg# of its whole-rock composition (calculated with $Fe^{3+}/Fe^T = 0.24$, analyzed in olivine-hosted melt inclusions in Big Pine basalts; Kelley and Cottrell, 2012). Bars on LV samples represent the propagated effect on Mg# for a variance of ±0.03 in the Fe^{3+}/Fe^T value. Also shown are samples from Big Pine (Brehm and Lange, 2020) and the Tancítaro volcanic field, along an active Mexican arc (TVF; Pu et al., 2017). Samples are superimposed over isopleths of $^{Fe2+Mg}K_D$ (olivine–melt). All LV samples from this study but one (#70, highlighted in grey) fall on K_D isopleths that range from 0.32–0.36 (expected values; Table 1) and thus pass the K_D liquidus test.

Table 3a
$^{Fe2+-Mg}K_D$ (olivine–melt) at liquidus with predicted values from literature.

Calculated $^{Fe2+-Mg}K_D$ (olivine–melt)	#69	#52	#147	#95	#23	#90	#67	#70	#129
MELTS (NNO)[a]	0.32	0.33	0.30	0.30	0.34	0.34	0.32	0.29	0.31
Putirka '16[b]	0.32	0.33	0.33	0.33	0.33	0.33	0.33	0.33	0.33
This study[c]	0.34	0.35	0.36	0.32	0.35	0.36	0.36	*0.39*	0.32
Diff: This study – P'16[d]	0.02	0.02	0.03	−0.01	0.02	0.03	0.03	*0.06*	−0.01

[a] Calculation of $^{Fe2+-Mg}K_D$ (olivine–melt) from MELTS (Ghiorso and Sack, 1995; Asimow and Ghiorso, 1998).
[b] Calculation of $^{Fe2+-Mg}K_D$ (olivine–melt) from Putirka (2016).
[c] Calculation of $^{Fe2+-Mg}K_D$ (oliv–melt) at liquidus from data in Tables 1 and 2; melt $Fe^{3+}/Fe^T = 0.24$.
[d] Difference between values obtained with Putirka (2016) calculation and this study. Results for sample #70 in italics, see Section 5.1.2 for application of olivine–melt liquidus test.

Table 3b
Comparison of $^{Mn-Mg}K_D$ (olivine–melt) at liquidus with predicted values from literature.

Calculated $^{Mn-Mg}K_D$ (olivine–melt)	#69	#52	#147	#95	#23	#90	#67	#70	#129
Blundy '20[a]	0.21	0.21	0.20	0.20	0.20	0.20	0.21	0.21	0.19
This study[b]	0.21	0.18	0.19	0.18	0.20	0.19	0.25	0.25	0.18
Diff: This study – B'20[c]	0.00	−0.03	−0.01	−0.02	0.00	−0.01	0.04	0.04	−0.01

[a] Calculation of $^{Mn-Mg}K_D$ (olivine–melt) from Blundy et al. (2020, Eq. 10); using T_{Ni} (Table 2, this study).
[b] Measured $^{Mn-Mg}K_D$ (olivine–melt) at liquidus from data in Tables 1 and 2.
[c] Difference between values obtained with Blundy et al. (2020, Eq. 10) calculation and this study.

crystal (±0.01 wt%). Within this analytical uncertainty of ~0.03, there is excellent agreement for all samples (but two), with differences of ≤0.03 between measured values (this study; Table 3b) and those calculated from the model of Blundy et al. (2020). The exceptions are samples #67 and #70, for which the $^{Mn-Mg}K_D$ (olivine–melt) values deviate by 0.04 (Table 3b). These results fully support the conclusions drawn on the basis of the $^{Fe^{2+}-Mg}K_D$ (olivine–melt) liquidus test (Table 3a; Fig. 14), and they additionally show internal consistency with the olivine–melt thermometry results obtained in this study, which are based on the Ni-thermometer of Pu et al. (2017, 2021).

5.5. Maximum pressure (depth) at onset of clinopyroxene growth

Clinopyroxene phenocrysts were analyzed in the three most Mg-rich LV basalts, and in two of them (#52 and #147), the most Cr- and Mg-rich composition was found in dark un-zoned cores (Table 4). When each pyroxene composition is paired with its respective whole-rock composition, the resulting $^{Fe^T-Mg}K_D$ value (Table 4; where Fe^T refers to total iron in both pyroxene and melt) overlaps the range predicted for clinopyroxene–liquid Fe–Mg exchange equilibrium (0.27± 0.03; Putirka, 2008) and suggests that clinopyroxene closely followed olivine as a crystallizing phase in these two cases. An estimate of the maximum depth for the onset of clinopyroxene crystallization in these two samples can be obtained by applying the Neave and Putirka (2017) clinopyroxene–melt geobarometer. Calculated pressures increase with temperature and the MgO content of the melt. Therefore, by applying T_{Ni} (the temperature at the onset of olivine crystallization) and the whole-rock composition, a maximum depth for the onset of clinopyroxene is determined. The results show that the dark, unzoned cores in clinopyroxene began to crystallize at pressures ≤0.54 GPa (CPX 22, #147) and ≤0.45 GPa (CPX 6; #52). These results confirm that there is no evidence of clinopyroxene crystallization at lower

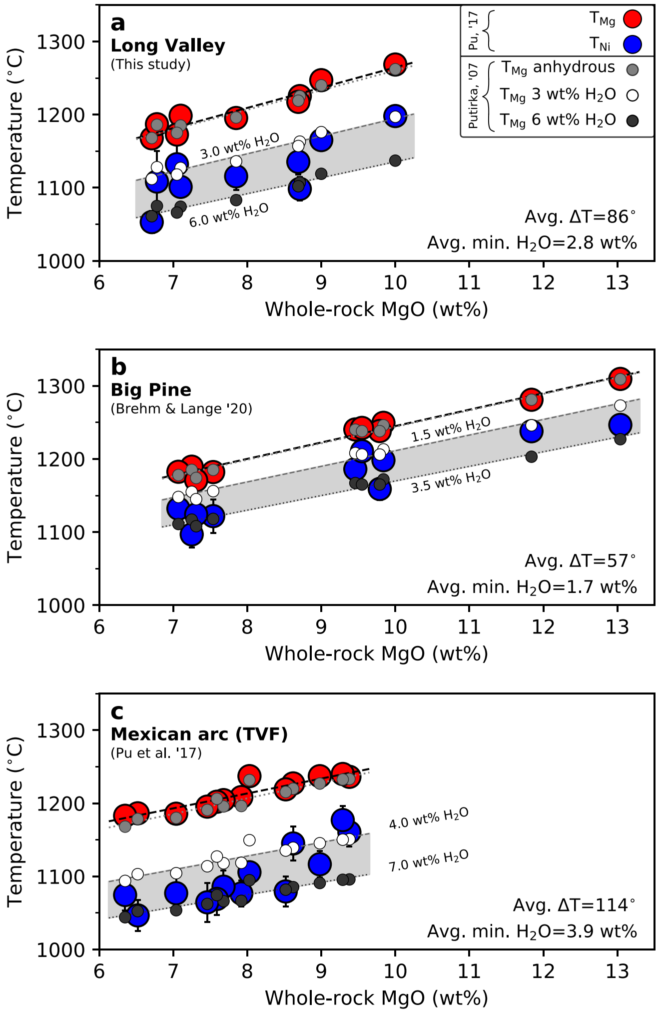

Fig. 15. Calculated temperatures (°C) from olivine–melt Mg- and Ni-thermometers (T_{Mg} and T_{Ni}, respectively) from Pu et al. (2017) versus whole-rock MgO (wt%) along with T_{Mg} from Putirka et al. (2007) calculated at anhydrous and various H_2O contents. (a) LV basalts from this study, (b) Big Pine basalts (Brehm and Lange, 2020), and (c) Tancítaro volcanic field from the Mexican arc (TVF; Pu et al., 2017). Both T_{Mg} and T_{Ni} increase linearly with increasing whole-rock MgO (wt%). Larger ΔT values (larger suppression of olivine liquidus temperatures due to dissolved water) reflect higher water contents. Note that the average ΔT (=T_{Mg}–T_{Ni}) for the Long Valley basalts (86 °C) is between the average ΔT for Big Pine and the TVF (57 °C and 114 °C, respectively), which suggests the LV basalts contained an average water content between those reported for the Big Pine basalts (≤3 wt%; Gazel et al., 2012) and TVF basalts (≤5.7 wt%; Johnson et al., 2009). This conclusion is also supported by T_{Mg} values calculated with the Putirka et al. (2007) thermometer, where H_2O contents of 3–6, 1.5–3.5, and 4–7 wt% recover T_{Ni} temperatures (Pu et al., 2017) for LV, Big Pine, and TVF basalts, respectively.

crustal depths in the LV basalts, unlike the case for the Big Pine basalts (Mordick and Glazner, 2006; Brehm and Lange, 2020).

In sample #69, only sector- and oscillatory-zoned clinopyroxene crystals are found. When one of the most Mg-rich clinopyroxenes (CPX 16) is paired with the whole-rock composition, the resulting $^{Fe^T-Mg}K_D$ value of 0.39 (a value too high for equilibrium, confirming pyroxene is not a near-liquidus phase) and a maximum depth of ≤0.19 GPa is obtained. This result underscores the conclusion drawn in Brehm and Lange (2020) that sector- and oscillatory-zoned clinopyroxenes in basalts form by rapid, degassing-induced crystallization in the upper crust after fluid saturation during ascent has occurred.

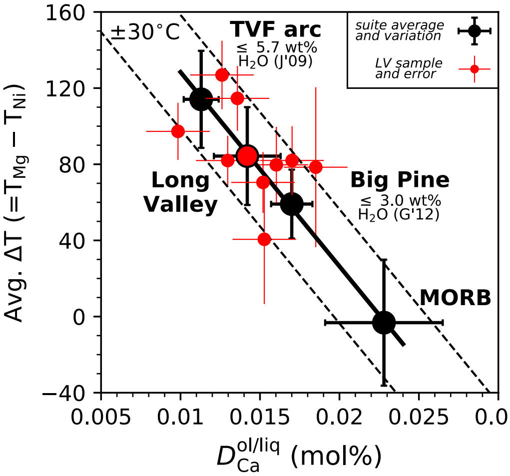

Fig. 16. Average ΔT (=T_{Mg}–T_{Ni}) versus mol% $D_{Ca}^{ol/liq}$ for Long Valley basalts (this study), Big Pine basalts (Brehm and Lange, 2020), TVF arc basalts (Pu et al., 2017), and MORBs (Allan et al., 1989; Pu et al., 2017). Larger ΔT (and thus higher melt H_2O, due to its suppression of olivine liquidus) correlates negatively with mol% $D_{Ca}^{ol/liq}$, where lower values are associated with higher melt water contents (e.g. Gavrilenko et al., 2016). Large symbols with capped bars denote suite average and sample variation. Note that results for individual LV basalts (small red circles with uncapped bars denoting propagated error) plot along the trend line within the ±30°C dashed error bars.

Table 4

Max Mg# clinopyroxene composition (wt%) and max cpx–liquid barometry results.

Sample Crystal Texture	#69 CPX 16 Sector zoned	#52 CPX 6 Dark core	#147 CPX 22 Dark core
SiO_2	51.71	52.85	50.95
TiO_2	0.72	0.24	0.50
Al_2O_3	2.82	2.53	3.94
FeO^T	5.27	4.18	4.83
MnO	0.11	0.11	0.10
MgO	16.83	18.31	16.85
CaO	22.39	20.42	21.06
Na_2O	0.24	0.55	0.53
Cr_2O_3	0.43	1.14	1.01
Mg#	85.1	88.7	86.1
Clinopyroxene–liquid barometry[a]			
$^{Fe^T-Mg}K_D$ (cpx–liquid)	0.39	0.27	0.28
P (GPa), T_{Ni} (°C)[b]		0.45, 1155	0.54, 1092
Depth (km)[c]		17	20

[a] Calculated with Neave and Putirka (2017) model; whole-rock for liquid composition.
[b] T_{Ni} from Table 2.
[c] Average crustal density of 2.75 g/cm^3 assumed.

6. Conclusions and implications

There are several major findings and key conclusions that can be drawn from this study. First and foremost, the high-MgO (6.7–9.9 wt%) LV basalts examined in this study contain olivine and clinopyroxene phenocrysts that display diffusion-limited, rapid-growth textures, consistent with crystallization during ascent (along fractures) to the surface. Moreover, eight of nine of these basalts contain an olivine phenocryst population where the most Mg-rich composition matches that expected for the liquidus of the whole-rock composition. In other words, the most Mg-rich olivine passes the $^{Fe^{2+}-Mg}K_D$ (olivine–melt) and $^{Mn-Mg}K_D$

(olivine–melt) liquidus tests (e.g., Putirka, 2016; Blundy et al., 2020), which indicates that the first olivine to crystallize in each basaltic liquid is closely represented by the most Mg-rich olivine analyzed in each sample.

Another major finding is that application of the Ni-based olivine–melt thermometer of Pu et al. (2017), which requires no corrections for melt water content, gives temperatures that range from 1198 to 1053 °C for the onset of olivine growth during ascent. Additionally, when the Mg-thermometer from Pu et al. (2017) is additionally applied, which gives the temperature under anhydrous conditions, the difference between T_{Mg} and T_{Ni} gives the magnitude of the suppression of the liquidus due to dissolved water in the melt. The average ΔT ($=T_{Mg}-T_{Ni}$) for all nine LV basalts is 86 ($\pm$27) °C and corresponds to an average minimum water content of ~2.8 wt% (Pu et al., 2017). When the H_2O-corrected olivine–melt thermometer of Putirka et al. (2007) is applied, the average amount of H_2O required to match the T_{Ni} values is ~4.3 ($\pm$1.5) wt%. The water contents in the LV basalts are lower than those in basalts erupted from the Mexican arc (e.g., ≤5.7 wt% H_2O in Mexican arc; Johnson et al., 2009), but higher than those in the Big Pine basalts (1.5–3.0 wt% H_2O; Gazel et al., 2012). The higher water contents in the LV basalts are consistent with their higher Ba/La ratios (indicative of slab-derived fluid signature) relative to those in the Big Pine basalts (Fig. 2b).

Finally, clinopyroxene phenocrysts in the three most Mg-rich LV basalts did not begin to crystallize until upper crustal depths (<0.5 GPa). The absence of clinopyroxene crystallization in the LV basalts during transit through the lower crust, which did occur in several Big Pine basalts, may also reflect the role that the higher water contents in the LV basalts played in suppressing the clinopyroxene liquidus at those depths.

Funding

This study was supported by the National Science Foundation (Grants EAR-1551344 and EAR-1855751).

Declaration of Competing Interest

The authors declare that they have no known competing financial interests or personal relationships that could have appeared to influence the work reported in this paper.

Acknowledgements

We thank Dr. Owen Neill for his expertise and assistance in obtaining high-quality X-ray intensity maps on the electron microprobe. Constructive reviews from Drs. Yannick Le Moigne and Keith Putirka improved the paper and are greatly appreciated. We additionally thank Drs. Gordon Moore, Adam Simon, and Youxue Zhang for their helpful comments on an earlier version of this manuscript.

Appendix A. Supplementary data

Supplementary data to this article can be found online at https://doi.org/10.1016/j.jvolgeores.2021.107298.

References

Allan, J.F., Batiza, R., Perfit, M.R., Fornari, D.J., Sack, R.O., 1989. Petrology of lavas from the Lamont Seamount Chain and adjacent East Pacific rise, 10°N. J. Petrol. 30, 1245–1298.

Almeev, R.A., Holtz, F., Koepke, J., Parat, F., Botcharnikov, R.E., 2007. The effect of H_2O on olivine crystallization in MORB: experimental calibration at 200 MPa. Am. Mineral. 92, 670–674.

Andersen, N.L., Jicha, B.R., Singer, B.S., Hildreth, W., 2017. Incremental heating of Bishop Tuff sanidine reveals pre-eruptive radiogenic Ar and rapid remobilization from cold storage. Proc. Natl. Acad. Sci. U. S. A. 114 (47), 12407–12412.

Anderson, A.T., Davis, A.M., Lu, F., 2000. Evolution of Bishop Tuff rhyolitic magma based on melt and magnetite inclusions and zoned phenocrysts. J. Petrol. 41 (3), 449–473.

Asimow, P.D., Ghiorso, M.S., 1998. Algorithmic modifications extending MELTS to calculate subsolidus phase relations. Am. Mineral. 83 (9–10), 1127–1132.

Bailey, R.A., 1989. Geologic map of Long Valley caldera. Mono-Inyo craters volcanic chain, and vicinity, eastern California: US geological survey miscellaneous investigations map I-1933, scale, 1(62,500)p. 11.

Bateman, P.C., 1992. Plutonism in the central part of the Sierra Nevada batholith, California. U.S. Geol. Surv. Prof. Pap. 1483, 1–186.

Beard, B.L., Glazner, A.F., 1995. Trace element and Sr and Nd isotopic composition of mantle xenoliths from the big Pine volcanic field, California. J. Geophys. Res. 100, 4169–4179.

Beattie, P., 1993. Olivine-melt and orthopyroxene-melt equilibria. Contrib. Mineral. Petrol. 115, 103–111. https://doi.org/10.1007/BF00712982S.

Blundy, J., Melekhova, E., Ziberna, L., Humphreys, M.C.S., Cerantola, V., Brooker, R.A., McCammon, C.A., Pichavant, M., Ulmer, P., 2020. Effect of redox on Fe-Mg-Mn exchange between olivine and melt and an oxybarometer for basalts. Contrib. Mineral. Petrol. 175, 103. https://doi.org/10.1007/s00410-020-01736-7.

Brehm, S., Lange, R.A., 2020. Rapid phenocryst growth in xenolith-bearing basalts from the Big Pine volcanic field, CA: application of olivine-melt oxybarometry, thermometry, and hygrometry at the liquidus. Geochem. Geophys. Geosyst. 21. https://doi.org/10.1029/2020GC009264.

Brophy, J.G., Whittington, C.S., Park, Y.-R., 1999. Sector-zoned augite megacrysts in Aleutian high alumina basalts: implications for the conditions of basalt crystallization. Contrib. Mineral. Petrol. 135, 277–290.

Calogero, M.A., Hetland, E.A., Lange, R.A., 2020. High-resolution numerical modeling of heat and volatile transfer from basalt to wall rock: application to the crustal column beneath Long Valley caldera, CA. J. Geophys. Res. 125, e2018JB01673.

Cortés, J.A., Smith, E.I., Valentine, G.A., Johnsen, R., Rasoazoanamparany, C., Widom, E., Sas, M., Ruth, D., 2015. Intrinsic conditions of magma genesis at the Lunar Crater Volcanic Field (Nevada), and implications for internal plumbing and magma ascent. Am. Mineral. 100, 396–413.

Cousens, B.L., 1996. Magmatic evolution of Quaternary mafic magmas at Long Valley caldera and the Devils Postpile, California: Effects of crustal contamination on lithospheric mantle-derived magmas. J. Geophys. Res. 101 (B12), 27673–27689.

Donaldson, C.H., 1976. An experimental investigation of olivine morphology. Contrib. Mineral. Petrol. 57, 187–213.

Du Bray, E.A., John, D.A., Cousens, B.L., Hayden, L.A., Vikre, P.G., 2016. Geochemistry, petrologic evolution, and ore deposits of the Miocene Bodie Hills volcanic field, California and Nevada. Am. Mineral. 101 (3), 644–677.

Faure, F., Trolliard, G., Nicollet, C., Montel, J.-M., 2003. A developmental model of olivine morphology as a function of the cooling rate and the degree of undercooling. Contrib. Mineral. Petrol. 145, 251–263.

Gavrilenko, M., Herzberg, C., Vidito, C., Carr, M.J., Tenner, T., Ozerov, A., 2016. A calcium-in-olivine geohygrometer and its application to subduction-zone magmatism. J. Petrol. 57, 1811–1832.

Gazel, E., Plank, T., Forsyth, D.W., Bendersky, C., Lee, C.T.A., Hauri, E.H., 2012. Lithosphere versus asthenosphere mantle sources at the big Pine Volcanic Field, California. Geochem. Geophys. Geosyst. 13 (1), 1–25.

Ghiorso, M.S., Sack, R.O., 1995. Chemical mass transfer in magmatic processes IV. A revised and internally consistent thermodynamic model for the interpolation and extrapolation of liquid-solid equilibria in magmatic systems at elevated temperatures and pressures. Contrib. Mineral. Petrol. 119 (2–3), 197–212.

Halliday, A.N., Mahood, G.A., Holden, P., Metz, J.M., Dempster, T.J., Davidson, J.P., 1989. Evidence for long residence times for rhyolitic magma in the Long Valley magmatic system: the isotopic record in precaldera lavas of Glass Mountain. Earth Planet. Sci. Lett. 94, 274–290.

Herzberg, C., O'Hara, M.J., 2002. Plume-associated ultramafic magmas of Phanerozoic age. J. Petrol. 43, 1857–1883.

Hildreth, W., 1979. The Bishop Tuff: evidence for the origin of compositional zonation in silicic magma chambers. Geol. Soc. Am. Spec. Pap. 180, 43–75.

Hildreth, W., 2004. Volcanological perspectives on Long Valley, Mammoth Mountain, and Mono Craters: several contiguous but discrete systems. J. Volcanol. Geotherm. Res. 136, 169–198.

Hildreth, W., Wilson, C.J.N., 2007. Compositional zoning of the Bishop Tuff. J. Petrol. 48 (5), 951–999.

Housh, T.B., Aranda-Gómez, J.J., Luhr, J.F., 2010. Isla Isabel (Nayarit, México): quaternary alkalic basalts with mantle xenoliths erupted in the mouth of the Gulf of California. J. Volcanol. Geotherm. Res. 197 (1–4), 85–107.

Johnson, E.R., Wallace, P.J., Cashman, K.V., Granados, H.D., Kent, A.J.R., 2008. Magmatic volatile contents and degassing-induced crystallization at Volcán Jorullo, Mexico: Implications for melt evolution and the plumbing systems of monogenetic volcanoes. Earth Planet. Sci. Lett. 269 (3–4), 478–487.

Johnson, E.R., Wallace, P.J., Granados, H.D., Manea, V.C., Kent, A.J.R., Bindeman, I.N., Donegan, C.S., 2009. Subduction-related volatile recycling and magma generation beneath Central Mexico: insights from melt inclusions, oxygen isotopes and geodynamic models. J. Petrol. 50, 1729–1764.

Kelley, K.A., Cottrell, E., 2012. The influence of magmatic differentiation on the oxidation state of Fe in a basaltic arc magma. Earth Planet. Sci. Lett. 329–330, 109–121.

Kouchi, A., Sugawara, Y., Kashmia, K., Sunagawa, I., 1983. Laboratory growth of sector zoned clinopyroxenes in the system $CaMgSi_2O_6$-$CaTiAl_2O_6$. Contrib. Mineral. Petrol. 83, 177–184.

Lange, R.A., Carmichael, I.S.E., 1996. The Aurora volcanic field, California–Nevada: oxygen fugacity constraints on the development of andesitic magma. Contrib. Mineral. Petrol. 125, 167–185.

Lange, R.A., Carmichael, I.S.E., Renne, P.R., 1993. Potassic volcanism near Mono basin, California: evidence for high water and oxygen fugacities inherited from subduction. Geology 21, 949–952.

Le Maitre, R.W., Streckeisen, A., Zanettin, B., Le Bas, M.J., Bonin, B., Bateman, P., 2005. Igneous Rocks: A Classification and Glossary of Terms: Recommendations of the International Union of Geological Sciences Subcommission on the Systematics of Igneous Rocks. 2nd ed. Cambridge University Press, Cambridge, U.K, p. 256.

Lofgren, G., 1974. An experimental study of plagioclase crystal morphology; isothermal crystallization. Am. J. Sci. 272, 243–273.

Manley, C.R., Glazner, A.F., Farmer, G.L., 2000. Timing of volcanism in the Sierra Nevada of California: evidence for Pliocene delamination of the basaltic root? Geology 28 (9), 811–814.

Médard, E., Grove, T.L., 2008. The effect of H_2O on the olivine liquidus of basaltic melts: experiments and thermodynamic models. Contrib. Mineral. Petrol. 155, 417–432.

Metz, J.M., Mahood, G.A., 1991. Development of the Long Valley, California, magma chamber recorded in precaldera rhyolite lavas of Glass Mountain. Contrib. Mineral. Petrol. 106, 379–397.

Milman-Barris, M.S., Beckett, J.R., Baker, M.B., Hofmann, A.E., Morgan, Z., Crowley, M.R., Stolper, E., 2008. Zoning of phosphorus in igneous olivine. Contrib. Mineral. Petrol. 155 (6), 739–765.

Miyashiro, A., 1978. Nature of alkalic volcanic rock series. Contrib. Mineral. Petrol. 66, 91–104.

Mordick, B.E., Glazner, A.F., 2006. Clinopyroxene thermobarometry of basalts from the Coso and big Pine volcanic fields, California. Contrib. Mineral. Petrol. 152 (1), 111–124.

Neave, D.A., Putirka, K.D., 2017. A new clinopyroxene-liquid barometer, and implications for magma storage pressures under Icelandic rift zones. Am. Mineral. 102, 777–794.

Norman, M.D., Garcia, M.O., 1999. Primitive magmas and source characteristics of the Hawaiian plume: petrology and geochemistry of shield picrites. Earth Planet. Sci. Lett. 168, 1–2.

Pu, X., Lange, R.A., Moore, G.M., 2017. A comparison of olivine-melt thermometers based on D_{Mg} and D_{Ni}: the effects of melt composition, temperature, and pressure with applications to MORBs and hydrous arc basalts. Am. Mineral. 102 (4), 750–765.

Pu, X., Moore, G.M., Lange, R.A., Touran, J.P., Gagnon, E., 2021. Experimental evaluation of a new H_2O-independent thermometer based on olivine-melt Ni partitioning at crustal pressure. Am. Mineral. 106 (February issue).

Putirka, K.D., 2008. Thermometers and barometers for volcanic systems. Rev. Mineral. Geochem. 69, 61–120.

Putirka, K.D., 2016. Rates and styles of planetary cooling on Earth, Moon, Mars, and Vesta, using new models for oxygen fugacity, ferric-ferrous ratios, olivine-liquid Fe-Mg exchange, and mantle potential temperature. Am. Mineral. 101, 819–840.

Putirka, K.D., Perfit, M., Ryerson, F.J., Jackson, M.G., 2007. Ambient and excess mantle temperatures, olivine thermometry, and active vs. passive upwelling. Chem. Geol. 241 (3–4), 177–206.

Putirka, K.D., Jean, M., Cousens, B., Sharma, R., Torrez, G., Carlson, C., 2012. Cenozoic volcanism in the Sierra Nevada and Walker Lane, California, and a new model for lithosphere degradation. Geosphere 8 (2), 265–291.

Roberge, J., Wallace, P.J., Kent, A.J.R., 2013. Magmatic processes in the Bishop Tuff rhyolitic magma based on trace elements in melt inclusions and pumice matrix glass Contributions to Mineralogy and Petrology. vol. 165 pp. 237–257.

Saleeby, J., Ducea, M., Clemens-Knott, D., 2003. Production and loss of high-density batholitic root, southern Sierra Nevada, California. Tectonics 22 (6), 1064.

Shea, T., Hammer, J.E., Hellebrand, E., Mourey, A.J., Costa, F., First, E.C., Lynn, K.J., Melnik, O., 2019. Phosphorous and aluminum zoning in olivine: contrasting behavior of two nominally incompatible trace elements. Contrib. Mineral. Petrol. 174 (85), 1–24.

Shimizu, N., 1990. The oscillatory trace element zoning in augite phenocrysts. Earth Sci. Rev. 29, 27–37.

Simkin, T., Smith, J.V., 1970. Minor-element distribution in Olivine. J. Geol. 78, 3.

Simon, J.I., Weis, D., DePaolo, D.J., Renne, P.R., Mundil, R., Schmitt, A.K., 2014. Assimilation of preexisting Pleistocene intrusions at Long Valley by periodic magma recharge accelerates rhyolite generation: rethinking the remelting model. Contrib. Mineral. Petrol. 167, 955.

Skulski, T., Minarik, W., Watson, E.B., 1994. High-pressure experimental trace-element partitioning between clinopyroxene and basaltic melts. Chem. Geol. 117, 127–147.

Ubide, T., Mollo, S., Zhao, J., Nazzari, M., Scarlato, P., 2019. Sector-zoned clinopyroxene as a recorder of magma history, eruption triggers, and ascent rates. Geochim. Cosmochim. Acta 251, 265–283.

Wallace, P.J., Anderson, A.T., Davis, A.M., 1999. Gradients in H_2O, CO_2, and exsolved gas in a large-volume silicic magma system: interpreting the record preserved in melt inclusions from the Bishop Tuff. J. Geophys. Res. 104 (B9), 20097–20122.

Welsch, B., Faure, F., Famin, V., Baronnet, A., Bachelery, P., 2013. Dendritic crystallization: a single process for all the textures of olivine in basalts? J. Petrol. 54, 539–574.

Welsch, B., Hammer, J., Hellebrand, E., 2014. Phosphorus zoning reveals dendritic architecture of olivine. Geology 42 (10), 867–870.

Welsch, B., Hammer, J., Baronnet, A., Jacob, S., Hellebrand, E., Sinton, J., 2016. Clinopyroxene in postshield Haleakala ankaramite. 2. Texture, compositional zoning and supersaturation in the magma. Contrib. Mineral. Petrol. 171, 6.

Zandt, G., Hersh, G., Owens, T.J., Ducea, M., Saleeby, J., Jones, C.H., 2004. Active foundering of a continental arc root beneath the southern Sierra Nevada in California. Nature 431 (7004), 41–46. https://doi.org/10.1038/nature02847.